

End-to-end Differentiable Calibration and Reconstruction for Optical Particle Detectors

Omar Alterkait,^{1,2,*} César Jesús-Valls,^{3,†} Ryo Matsumoto,⁴ Patrick de Perio,⁵ and Kazuhiro Terao⁶

¹*Department of Physics and Astronomy, Tufts University, 574 Boston Ave, Medford, MA 02155, USA*

²*The NSF AI Institute for Fundamental Interactions, MIT, Cambridge, MA 02139, USA*

³*European Organization for Nuclear Research (CERN), 1211 Geneva 23, Switzerland*

⁴*Department of Physics, Institute of Science Tokyo, Meguro, Tokyo 152-8551, Japan*

⁵*Center for Data-Driven Discovery, Kavli IPMU (WPI), UTIAS,*

The University of Tokyo, Kashiwa, Chiba 277-8583, Japan

⁶*SLAC National Accelerator Laboratory, Menlo Park, CA, 94025, USA*

Large-scale homogeneous detectors with optical readouts are widely used in particle detection, with Cherenkov and scintillator neutrino detectors as prominent examples. Analyses in experimental physics rely on high-fidelity simulators to translate sensor-level information into physical quantities of interest. This task critically depends on accurate calibration, which aligns simulation behavior with real detector data, and on tracking, which infers particle properties from optical signals. We present the first end-to-end differentiable optical particle detector simulator, enabling simultaneous calibration and reconstruction through gradient-based optimization. Our approach unifies simulation, calibration, and tracking, which are traditionally treated as separate problems, within a single differentiable framework. We demonstrate that it achieves smooth and physically meaningful gradients across all key stages of light generation, propagation, and detection while maintaining computational efficiency. We show that gradient-based calibration and reconstruction greatly simplify existing analysis pipelines while matching or surpassing the performance of conventional non-differentiable methods in both accuracy and speed. Moreover, the framework’s modularity allows straightforward adaptation to diverse detector geometries and target materials, providing a flexible foundation for experiment design and optimization. The results demonstrate the readiness of this technique for adoption in current and future optical detector experiments, establishing a new paradigm for simulation and reconstruction in particle physics.

I. INTRODUCTION

Large-scale homogeneous particle detectors with optical readouts are a cornerstone of modern particle physics research. Prominent examples include neutrino detectors such as Super-Kamiokande [1], SNO [2], KamLAND [3], Borexino [4], Daya Bay [5], IceCube [6] and KM3Net [7] and JUNO [8]. This technology has critically shaped our modern understanding of neutrino physics [9–26]. Several of these experiments remain operational or are entering new phases with enhanced capabilities, and are expected to continue delivering leading results in the coming decades. In parallel, next-generation experiments such as Hyper-Kamiokande [27] and proposed technologies for DUNE Phase II [28] will further extend the reach of this detector paradigm, collectively shaping the future of the field.

Like most other particle detectors, these types of detectors rely on physics simulators to translate detector-level information, such as sensor readings, into physics observables, such as the type of observed particles and their kinematics. The conventional procedure consists of three strongly co-dependent parts:

- **Simulation:** A digital replica of the experiment aiming to generate detector-level information analogous to the real detector.
- **Calibration:** A method that utilizes data collected under well-known conditions to align the simulation description to the detector behavior.
- **Reconstruction:** An algorithm that utilizes simulation predictions to infer physics observables from detector-level data.

A persistent challenge in particle physics is that existing detector simulators are designed as prediction-only tools without built-in parameter optimization, necessary for calibration and reconstruction tasks. The prevalence of this approach is illustrated by the fact that GEANT4 [29], the simulation toolkit used to develop such simulators, is the most citedⁱ article in experimental particle physics. The state-of-the-art methodology is, and has been for decades, to develop separate calibration and reconstruction solutions utilizing the detector simulation as needed, typically in a sequence of disjoint steps. This approach introduces artificial task divisions that contribute to inefficient workflows and prevent fully accounting for parameter correlations that contribute to data-simulation mismatches and poor understanding of

* Omar.Alterkait@tufts.edu

† Cesar.Jesus@cern.ch

ⁱ According to the INSPIRE HEP portal.

the underlying physics processes. This affects the ultimate experimental measurement robustness and sensitivity.

In this work, we demonstrate how a differentiable simulator bridges the gap between detector modeling and data analysis, transforming traditionally discrete and independent procedures into a single, continuous, and optimizable pipeline. Focusing on optical detectors, we showcase the first end-to-end differentiable simulator combining the necessary physics fidelity and computational efficiency to be readily applicable to existing and planned physics experiments.

This work represents a significant step toward the establishment of a new paradigm in experimental particle physics, with the potential to supersede existing approaches in terms of simplicity, efficiency, and robustness, while enabling new strategies for detector design optimization and uncertainty estimation.

A. Differentiable Simulations

Data analysis in particle physics is fundamentally an inverse problem. Given a set of observed sensor readouts, one seeks to infer the latent physical parameters, such as particle momenta or detector properties, that generated them. In the standard paradigm, this inference relies on forward simulations like GEANT4 [29] to maximize a likelihood or minimize a loss function. Since standard simulators function as non-differentiable black boxes, this optimization typically relies on discrete grid searches, derivative-free algorithms, or finite-difference approximations.

This approach suffers severely from the *curse of dimensionality*. As the number of parameters increases, the volume of the search space grows exponentially. Computing gradients via finite differences becomes prohibitively expensive because it requires running the full simulation at least once for every single parameter. Consequently, experimental workflows are forced to adopt a sequential calibration strategy. Subsets of parameters, such as geometry, optical properties, and electronics response, are tuned independently in a fixed order. This sequential treatment ignores the complex correlations between parameters. For instance, a bias in the absorption length might be compensated by a shift in photosensor efficiency, leading to suboptimal working points and systematic uncertainties that are difficult to quantify.

Differentiable programming offers a robust solution to these challenges by rendering the simulation code itself differentiable. This paradigm leverages Automatic Differentiation (AD) [30], a technique distinct from both symbolic differentiation and numerical finite differences. AD decomposes a computer program into a sequence of elementary operations and applies the chain rule of calculus to propagate and combine partial derivatives through each operation in order to obtain the overall derivative. This allows the exact gradient of the simulation output

with respect to any input parameter to be computed efficiently. Crucially, in reverse-mode AD, the computational cost of evaluating the full gradient vector is roughly constant regardless of the number of input parameters.

A powerful feature of this paradigm is the ability to construct hybrid models. Well-understood physical laws, such as ray optics, can be implemented as differentiable operators to maintain interpretability, while complex or computationally expensive microscopic processes can be approximated by neural networks. This allows the simulation to retain the expressiveness and efficiency of machine learning without sacrificing the physics processes of the experiment.

The adoption of differentiable programming is rapidly expanding within high-energy physics. The MODE collaboration has formalized the potential of this paradigm for end-to-end optimization, proposing that hardware design and reconstruction algorithms should be optimized simultaneously to maximize physics sensitivity [31]. At the fundamental physics level, tools like MADJAX have introduced differentiable matrix elements to incorporate theory parameters directly into gradient-based pipelines [32]. Similar techniques have been applied to jet physics to enable gradient-based variational inference over latent clustering histories [33], and to statistical analysis pipelines to optimize selection cuts directly for significance [34].

In the domain of detector simulation, significant progress has been made for Liquid Argon Time Projection Chambers (LArTPCs). Recent work has demonstrated a fully differentiable LArTPC simulator capable of simultaneously calibrating entangled detector parameters, such as electron drift and signal induction, using gradient descent [35].

This work is the first to focus on large-scale homogeneous optical detectors. To the best of our knowledge, it presents the first end-to-end differentiable simulation framework capable of jointly addressing calibration and reconstruction tasks within a single optimization pipeline, while achieving competitive computational efficiency and physics performance relative to established non-differentiable approaches.

B. Optical Particle Detectors

Most optical particle detectors rely on the detection and characterization of either Cherenkov light, scintillation light, or a combination of both. Cherenkov radiation occurs when charged particles traverse a medium with velocity v exceeding the local phase velocity of light, defined by $v > c/n$, where n is the refractive index. This process produces photons emitted instantaneously along a cone with half-opening angle θ_c satisfying $\cos\theta_c = c/(nv)$. Scintillation light, in contrast, is emitted isotropically, with an intensity and time profile that depends on the local energy deposition and the detector medium properties.

Optical detectors measure the spatial and temporal distribution of emitted photons using large volumes of transparent material instrumented with arrays of photosensors. This technology has proven particularly powerful in neutrino physics, enabling the construction of large, homogeneous, and cost-effective detectors.

Cherenkov detectors can distinguish the flavor of charged leptons produced in neutrino interactions by reconstructing the geometric pattern of Cherenkov light on the photosensor array. This capability has been central to studies of neutrino oscillations and provides directional sensitivity to the incoming neutrino, which is crucial for observations of atmospheric, solar, and supernova neutrinos.

Scintillation detectors primarily function as calorimeters, measuring the total energy deposited by particles through isotropic photon emission. They require precise modeling of scintillation yield, quenching effects, and de-excitation time.

II. END-TO-END DIFFERENTIABLE SIMULATION

We developed a JAX-based open-source **Light-based Unified Calibration and tracking Differentiable simulation, LUCiD**ⁱⁱ.

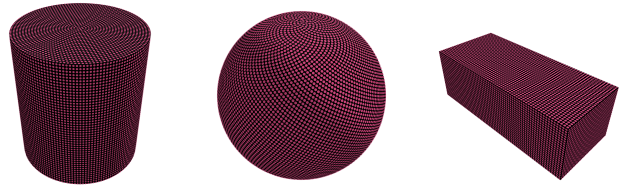
LUCiD serves as a demonstrator of an end-to-end differentiable simulation. It provides utilities to describe the detector geometry, photon generation, propagation through the detector medium, and hit formation while preserving differentiability throughout the entire pipeline. This section reviews these core components. In sections III and IV, we then illustrate how gradient information can be leveraged to perform gradient-based optimization for calibration and track reconstruction.

JAX was chosen as the core framework guided by the intention to build a robust and flexible system capable of accommodating the varied needs of different experiments and serving as a common tool for the broader community. Its automatic differentiation capabilities enable the exact computation of gradients through arbitrarily complex operations, a crucial feature for end-to-end optimization. JAX also provides just-in-time compilation and vectorization, ensuring efficient execution on both CPUs and GPUs while supporting large-scale parallelization. Its functional programming paradigm and composable design make it straightforward to adapt and extend to the specific needs of individual experiments.

A. Detector Geometry

We consider optical detectors defined by a physical boundary enclosing an inner volume and instrumented

FIG. 1. Examples of three detector geometries built parametrically using LUCiD.



with photosensors distributed along the surface. These assumptions enable modeling of the three most common geometries used in current and future optical neutrino detectors, namely cylinders, spheres, and rectangular boxes, with arbitrary size, material, and proportions.

The principles that ensure differentiability throughout the entire simulation chain are inherently geometry-agnostic. Therefore, extending this framework to other detector geometries does not require any conceptual modification, but rather the implementation of additional functionality.ⁱⁱⁱ This generality provides a solid foundation for developing a community-wide tool that can be readily adopted across experiments. Moreover, the differentiable nature of the simulation inherently enables built-in reconstruction for any detector configuration, naturally supporting efficient detector design optimization, as discussed in Sec. V.

Figure 1 illustrates three example geometry types implemented in LUCiD. Unless otherwise specified, results are presented for a cylindrical detector with parameters $R = 16.9$ m, $H = 36.2$ m, $s_R = 25$ cm, $N_s = 10764$, and c_{med} , corresponding respectively to the cylinder radius, height, sensor radius, number of sensors, and the speed of light in the detector medium. In this work, the medium is water, and we take $c_{\text{med}} = c/n$ with a refractive index $n = 1.33$. These values approximate the geometry of the Super-Kamiokande [1] detector; accordingly, we refer to this configuration as *SK-like*. For simplicity, all geometries are constructed parametrically by uniformly distributing sensors along the detector surface.

B. Modeling Expected Detector Responses

For calibration and reconstruction, LUCiD is designed to produce smoothed, differentiable expectations in detector-output space: predicted sensor responses that vary continuously with the underlying physical parameters and are suitable for gradient-based inference.

It is important to emphasize a conceptual distinction in objectives. Monte Carlo toolkits such as GEANT4 aim

ⁱⁱ <https://github.com/CIDeR-ML/LUCiD/>

ⁱⁱⁱ For example, the optimizations described in Sec. IID1 assume that photosensors are placed on a surface and would need to be generalized to three dimensions for geometries such as those of the IceCube [6] and KM3Net [7] experiments.

to generate individual events whose statistical properties match those of measured data by sampling physical photons and microscopic processes. By contrast, our simulator’s target quantity is the *expected* detector response (an “average event”) rather than individual stochastic realizations.

To represent these expectations we use *rays*, mathematical objects that encode averaged contributions (or superpositions) of many possible photon trajectories and outcomes. While it would be possible, in principle, to retain differentiability with an explicit photon-sampling approach, we choose rays because they directly represent the ensemble expectation we want to predict and because they facilitate variance-reduction during propagation, later discussed in Sec. II D. Each ray therefore need not correspond to a single physical photon; instead it carries an intensity and parameterization that together approximate the expected contribution of many photons. The intensity represents a fractional photon count. The user-specified parameter N_{rays} controls the granularity of this approximation, and individual ray intensities are automatically scaled to preserve the overall normalization of the expected signal. In this parameterization, the simulation approaches the continuous wave propagation limit as the number of rays approaches infinity.

This formulation does not alter the underlying physics that determines the optimal parameter values. In the high-statistics limit, a conventional sampling-based simulation would yield the same expected detector response and, consequently, the same loss minimum. The techniques introduced in subsequent sections serve distinct roles in making gradient-based optimization practical: implicit capture (Sec. II D) provides variance reduction, allowing the expectation to be estimated accurately with substantially fewer rays, while photon relaxation (Sec. II D 3) addresses discontinuities inherent to geometric ray-sensor intersection, ensuring that gradients remain well-defined and physically meaningful. The fundamental advantage of the differentiable framework is therefore twofold: reduced computational cost to evaluate the loss surface, and access to exact gradients that enable efficient optimization in high-dimensional parameter spaces.

C. Ray Generation

The goal of the ray-generation step is to construct a differentiable function that maps a set of physical parameters describing a charged-particle track or calibration configuration to a list of rays characterized by their emission position \mathbf{x}_γ , direction \mathbf{u}_γ , wavelength λ_γ , and time t_γ . Formally, we define

$$f_\gamma(\theta_{\text{event}}, \theta_{\text{detector}}) \rightarrow \{\mathbf{x}_i, \mathbf{u}_i, \lambda_i, t_i\}_{i=1}^{N_\gamma}, \quad (1)$$

where θ_{event} and θ_{detector} denote the event and detector parameters, respectively.

One approach to define f_γ is to describe all effects analytically using differentiable primitives, i.e. continuous mathematical operations that replicate the underlying physics while preserving gradient flow, an avenue we follow later when modeling ray propagation (see Sec. II D). However, re-implementing the complete set of microscopic effects is unnecessary for our use case. Since the physics governing the passage of particles through matter is well established and does not need to be optimized, representing f_γ through a surrogate model simplifies the implementation complexity and provides an opportunity to illustrate how differentiable simulators can be built combining analytical parametrizations and surrogate models.

We construct a differentiable surrogate for the Cherenkov light emission $f_\gamma^{\text{Cherenkov}}(E, s, \theta)$, which reproduces the expected photon emission distributions as a function of the initial particle energy E , photon emission distance along the track s , and emission angle θ . This parametrization is analogous to that used in FitQun [36], an official reconstruction software of the T2K, Super-Kamiokande and Hyper-Kamiokande experiments. To tune our surrogate, we first generate 3D lookup tables of $(E, s, \cos \theta)$ distributions using PHOTON-SIM^{iv}, a GEANT4-based utility developed for this purpose, and then train a Sinusoidal Representation Network (SIREN) [37] to interpolate them. Details of the model architecture and training procedure are provided in Appendix A. In this work, we do not consider polarization nor wavelength-dependent effects in either photon propagation or sensor response modeling, and therefore we do not include that information at the generation stage. Nevertheless, such second-order refinements can be naturally incorporated at the ray-generation level by extending the surrogate model following the same approach outlined above. For each ray i , random values of θ_i and s_i are drawn from uniform intervals^v, and a corresponding generation intensity

$$I_i^{\text{generation}} = f_\gamma^{\text{Cherenkov}}(E, \theta_i, s_i) \quad (2)$$

is assigned. This intensity is carried throughout the simulation chain, ensuring that the detector response remains differentiable with respect to the input particle energy.

With θ_i and s_i known for every ray, we compute the ray origin and direction as a function of the track parameters $\mathbf{x}_{\text{track}}$ and $\mathbf{u}_{\text{track}}$:

$$\mathbf{x}_\gamma = \mathbf{x}_{\text{track}} + s_i \mathbf{u}_{\text{track}}, \quad (3)$$

$$\mathbf{u}_\gamma = \cos \theta_i \mathbf{u}_{\text{track}} + \sin \theta_i (\cos \phi_i \hat{v} + \sin \phi_i \hat{w}), \quad (4)$$

where ϕ_i is a random azimuthal angle uniformly distributed in $[0, 2\pi)$, and \hat{v} and \hat{w} are orthonormal vectors

^{iv} <https://github.com/cesarjesusvalls/PhotonSim/>

^v Since $f^{\text{Cherenkov}}$ is quite sparse, we utilize an adaptive binning strategy to avoid sampling in regions where the intensities are zero, further details are presented in Appendix C.

perpendicular to $\mathbf{u}_{\text{track}}$ defining the local emission plane. These expressions correspond to rays emitted along a cone of opening angle θ_i around the particle trajectory, at a distance s_i from the track origin. Through these expressions, the rays predictions become continuous functions ensuring that the detector response remains differentiable with respect to the track origin and direction.

It is worth noting that this approach requires one surrogate model for each particle type (e.g. muons, electrons, pions, protons) and material of interest, resulting in a small set of lookup tables per experiment that need to be generated only once^{vi}. Producing the required lookup tables requires ~ 4 CPU days, while the subsequent SIREN training on GPU lasts for less than one hour.

The initial emission time t_0 can be described by the analytical parameterization

$$f_{\gamma}^{t_0}(E, s) = 10^{(\alpha_1 E + \beta_1)} \times s^{(\alpha_2 E + \beta_2)} + \xi, \quad (5)$$

where α_1 , α_2 , β_1 , β_2 , and ξ are fitted to predictions from PHOTONSIM. This expression refines the first-order estimate $t_0 = s/c$, with c the speed of light, by accounting for the slowdown of particles as they traverse the medium. Because the rate of energy loss depends on both particle type and material, each surrogate light-emission model must include a corresponding $f_{\gamma}^{t_0}$. The associated computing time to generate the necessary GEANT4 files is below 1 CPU hour.

FIG. 2. An example muon event generated with PHOTONSIM. The particle origin is denoted with a red star symbol and the photons creation time is indicated in color. A total of 1k photons chosen at random are also represented by arrows.

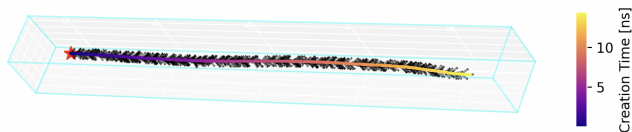
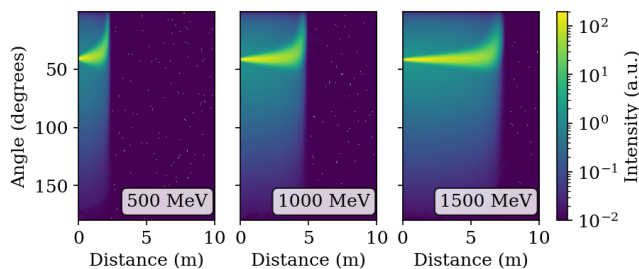
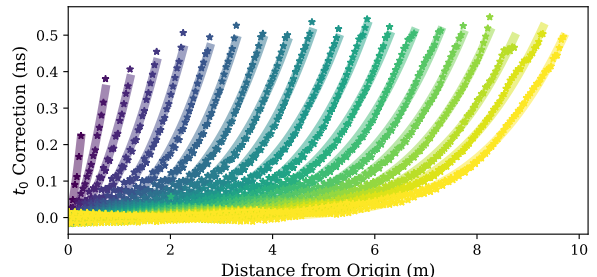


FIG. 3. Three example energy slices for the surrogate model of $f_{\gamma}^{\text{Cherenkov}}$ using muons.



^{vi} PHOTONSIM and LUCiD provide open-source utilities to generate the required GEANT4 photon samples, fit the surrogate models, and construct the corresponding emission-time parameterizations described later.

FIG. 4. Example of the parametrization of $f_{\gamma}^{t_0}$ for muons in water after subtracting $t_0 = s/c$, which accounts for the t_0 correction arising from the particle slowdown in the medium. Data points are shown as stars, with solid lines of matching colors representing the predictions from Eq. 5. From darker to lighter colors (left to right), the curves correspond to muon energies ranging from 100 MeV to 2000 MeV in steps of 100 MeV.



An example muon generated with PHOTONSIM is presented in Figure 2. Examples of $f_{\gamma}^{\text{Cherenkov}}$ and $f_{\gamma}^{t_0}$ for different energies are shown in Fig. 3 and Fig. 4.

The ray generation function for a particle can be generalized as a sum over all light-producing mechanisms:

$$f_{\gamma}^{\text{Particle}} = f_{\gamma}^{\text{Cherenkov}} + f_{\gamma}^{\text{Scintillation}}. \quad (6)$$

A strategy to model the emission of Cherenkov light along a particle path in a way that allows obtaining gradients for the particle parameters has been outlined above, and an analogous strategy could be employed to parameterize the emission of scintillation light, a task we envision for future work. Interested readers can find further comments in this regard in Appendix B.

The description of light emission by calibration sources, $f_{\gamma}^{\text{Calibration}}$, does not require parameterization as a function of a particle path, making it conceptually simpler. The calibration sources used in this work, namely an isotropic point source and a laser (see Sec. III), use equal intensities for all rays.

For the isotropic point source, all rays share the same origin and are distributed using a deterministic Fibonacci lattice [38] rather than pseudo-random sampling. The Fibonacci lattice places N points on the unit sphere according to

$$z_i = 1 - \frac{2i + 1}{N}, \quad (7)$$

$$\theta_i = 2\pi(i \cdot \varphi) \pmod{2\pi}, \quad (8)$$

where $i \in \{0, 1, \dots, N - 1\}$ and $\varphi = (\sqrt{5} - 1)/2 \approx 0.618$ is the golden ratio conjugate. The Cartesian coordinates follow as $x_i = \sqrt{1 - z_i^2} \cos \theta_i$, $y_i = \sqrt{1 - z_i^2} \sin \theta_i$. Unlike pseudo-random sampling, which suffers from non-uniform clustering, this quasi-Monte Carlo distribution provides highly uniform coverage of the sphere, significantly reducing the variance associated with finite sample sizes.

For the laser source, rays originate from the fiber tip position and are distributed uniformly in solid angle

within a cone. The maximum emission angle is determined by the fiber numerical aperture (NA) and the refractive index of the medium:

$$\theta_{\max} = \arcsin\left(\frac{\text{NA}}{n}\right). \quad (9)$$

To achieve uniform sampling in solid angle (rather than uniform in θ), we draw $u \sim \mathcal{U}[0, 1]$ and compute

$$\theta = \arcsin(\sqrt{u} \sin \theta_{\max}), \quad (10)$$

with the azimuthal angle ϕ sampled uniformly in $[0, 2\pi)$.

More sophisticated calibration sources could be implemented if needed, for example by modeling finite-sized or spatially non-uniform emitters, or by assigning position- or angle-dependent intensities to the rays.

D. Ray Propagation

We propagate rays through the detector medium using an analytic ray tracing approach. Unlike ray marching methods that discretize trajectories into small steps, our approach calculates exact intersection points with the detector geometry analytically. This ensures precision is limited only by floating-point arithmetic and allows the computational cost to scale with the number of interactions rather than the path length.

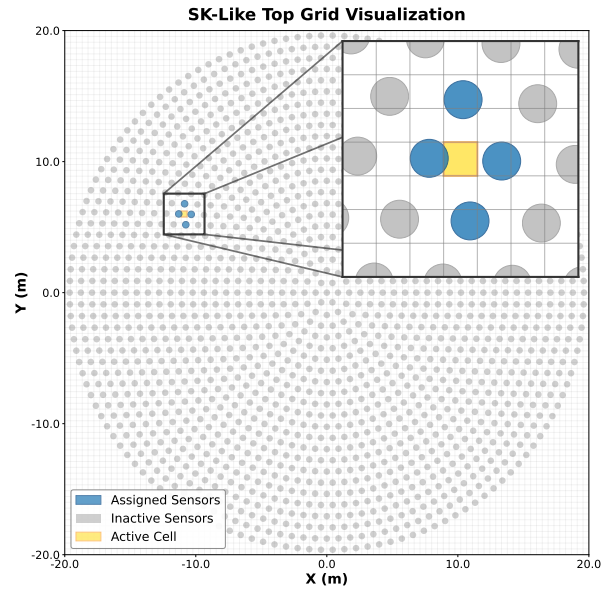
The propagation process is iterative. At each step k , up to a maximum K , we determine the ray collision point, evaluate the probabilities of competing physical processes (scattering, absorption, reflection, and detection), and update the ray state using differentiable operations.

1. Grid-accelerated Intersection

A naive intersection algorithm checks every ray against every photosensor, scaling linearly with the number of sensors $O(N_s)$. For existing large-scale experiments, involving thousands of photosensors, this is prohibitively expensive. We overcome this by implementing a spatially hashed grid system that reduces the complexity to $O(1)$.

For a given detector geometry, we discretize the surface into a grid of cells. During initialization, we precompute a mapping that assigns each grid cell a fixed list of up to M nearby sensors (typically $M = 4$), prioritized by geometric overlap and proximity. We model the photosensor enclosures as spheres to simplify these overlap calculations. During propagation, we first compute the analytic intersection of the ray with the global detector volume to obtain the surface intersection coordinates. These coordinates map directly to a specific grid cell, returning a candidate list of sensors that the ray may strike. This efficient reduction of the search space is illustrated in Fig. 5 for the top cap of a cylindrical detector. This two-stage approach yields the collision distance

FIG. 5. Visualization of the grid-based sensor lookup on the top cap of an SK-like detector. A single active grid cell is mapped to a specific subset of assigned sensors, allowing the intersection algorithm to ignore the remaining inactive sensors.



d_{coll} , the surface normal \mathbf{n} , and the indices of the specific sensors contributing to the hit.

2. Probabilistic Interactions and Variance Reduction

Given a ray traveling a distance d to a surface, we model the medium interactions using the scattering length λ_s and absorption length λ_a . The probability that a photon reaches the surface without scattering is $P_{\text{reach}} = \exp(-d/\lambda_s)$, while the probability of scattering is $P_{\text{scatter}} = 1 - P_{\text{reach}}$.

Standard Monte Carlo methods sample a binary outcome (scatter or reach) at this stage. To reduce variance and ensure smoother gradients, we employ *implicit capture*. Instead of terminating rays probabilistically, we deposit the expected probability weight directly into the sensor and attenuate the surviving ray. The ray carries an intensity I_i and a survival factor α_i . We calculate the attenuation due to absorption as $A(d) = \exp(-d/\lambda_a)$.

If the ray reaches the surface, it may reflect with probability R or be detected with probability $P_{\text{detect}} = P_{\text{reach}} \cdot (1 - R)$. We deposit a fraction of the ray intensity into the sensor:

$$n_{\text{dep}} = I_i \cdot \alpha_i \cdot P_{\text{detect}} \cdot A(d) \cdot w_{\text{geo}}, \quad (11)$$

where w_{geo} is a geometric overlap factor described in Sec. IID3. The ray then continues to propagate with its intensity scaled by the probability of the surviving paths (reflection or scattering) and their respective attenuation factors.

3. Photon Relaxation

A fundamental challenge in differentiable ray tracing is the binary nature of geometric intersection. Typically, the contribution of a ray to a sensor is defined by an indicator function which is 1 if the ray hits the sensor and 0 otherwise. This discontinuity prevents gradients from guiding rays toward sensors during optimization, as the gradient is zero almost everywhere.

Classic smooth relaxations, such as applying a sigmoid function to the signed distance, can address the discontinuity but often distort the effective sensor shape and underlying physics. We address this via *photon relaxation*, where we treat photons as having a spatial extent modeled by a Gaussian probability density function with width σ perpendicular to the propagation direction. The overlap weight w_{geo} corresponds to the integral of this Gaussian over the circular sensor area, represented by the purple region in Fig. 6. Exploiting the rotational symmetry, we precompute this integral as a function of the single impact parameter b , defined as the perpendicular distance from the ray to the sensor center, and store it as a differentiable lookup table. This formulation ensures that rays produce a nonzero, distance-dependent signal even when they strictly miss a sensor ($b > r$). Further details on the numerical implementation are provided in Appendix D 2.

4. Differentiable Path Sampling

To proceed to the next iteration, the ray must adopt a new position and direction. This involves two distinct types of stochasticity: continuous sampling of angles (e.g., scattering, reflection) and the discrete selection of the interaction type.

To enable differentiation, we apply the *reparameterization trick* [39]. In standard Monte Carlo simulations, sampling directly from a probability distribution breaks the computation graph (i.e., the sequence of operations through which derivatives are propagated), as the sampling operation is non-differentiable. The reparameterization trick circumvents this by rewriting the stochastic variable as a differentiable transformation of the distribution parameters and an independent source of noise. This effectively decouples the source of randomness (the noise) from the physical parameters (the transform); the optimizer views the noise as a fixed constant, treating the resulting photon state as a deterministic, differentiable function of the physics parameters.

For volumetric Rayleigh scattering, we avoid non-differentiable rejection sampling by using Inverse Transform Sampling (ITS). By equating the Rayleigh Cumulative Distribution Function (CDF) to a uniform noise sample $\epsilon \sim \mathcal{U}[0, 1]$, we obtain a cubic equation for the scattering angle cosine μ . We solve this analytically using Cardano’s formula, yielding a closed-form, differentiable mapping from noise to angle.

Upon reaching a boundary, we distinguish between surface types to demonstrate that different parameterizations can be used simultaneously within the same pipeline. We model the sensors as ideal specular surfaces to capture their glass-like reflectivity; here, the reflection direction is computed deterministically from the incident vector and surface normal. Conversely, we treat detector walls as Lambertian (diffuse) surfaces. For these, we reparameterize the standard cosine-weighted hemispherical sampling by transforming uniform noise into local angular coordinates. Both approaches allow gradients to propagate through the surface normals.

Finally, for the discrete categorical choice between volumetric scattering and surface interaction, standard sampling is non-differentiable. We resolve this using a vector-based Straight-Through Estimator (STE) [40]. Using the probabilities P_{reach} and P_{scatter} defined previously, we construct a normalized probability vector \mathbf{P} :

$$\mathbf{P} = \left[\frac{P_{\text{reach}}}{P_{\text{reach}} + P_{\text{scatter}}}, \frac{P_{\text{scatter}}}{P_{\text{reach}} + P_{\text{scatter}}} \right]. \quad (12)$$

We first sample a “one-hot” indicator vector $\mathbf{h} \in \{[1, 0], [0, 1]\}$ from \mathbf{P} to select a path. To restore differentiability, we calculate a surrogate weight vector \mathbf{w} that preserves the discrete selection in value but carries the probability gradients:

$$\mathbf{h} \sim \text{Categorical}(\mathbf{P}) \quad (13)$$

$$\mathbf{w} = \mathbf{h} - \text{sg}(\mathbf{P}) + \mathbf{P} \quad (14)$$

where $\text{sg}(\cdot)$ denotes the stop-gradient operator. The photon’s new position \mathbf{x} and direction \mathbf{u} are computed as linear combinations of the candidate outcomes using these weights:

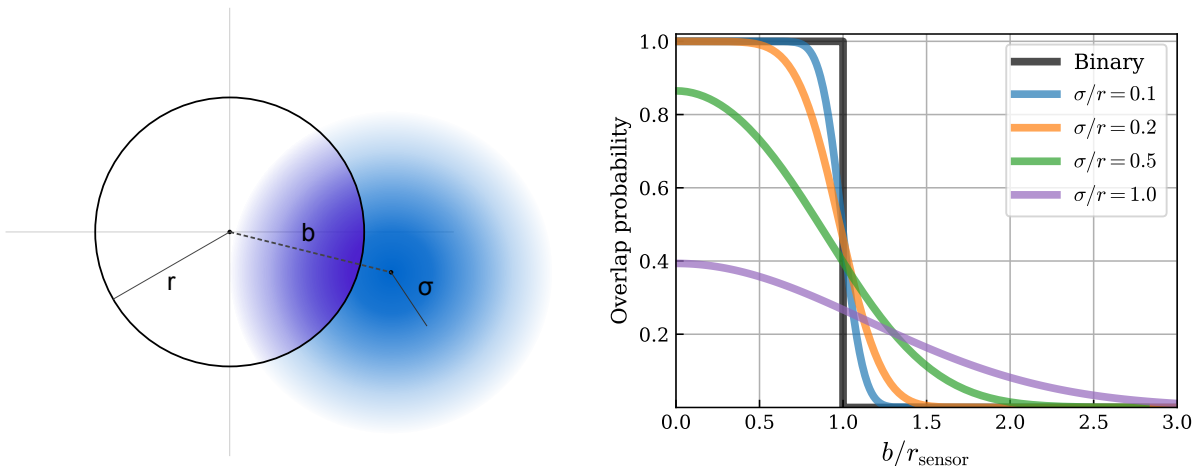
$$\mathbf{x}_{\text{new}} = w_0 \mathbf{x}_{\text{surf}} + w_1 \mathbf{x}_{\text{scat}} \quad (15)$$

$$\mathbf{u}_{\text{new}} = w_0 \mathbf{u}_{\text{surf}} + w_1 \mathbf{u}_{\text{scat}} \quad (16)$$

In the forward pass, $\mathbf{w} \equiv \mathbf{h}$, ensuring the photon geometrically adopts exactly one valid physical trajectory. In the backward pass, gradients flow through the continuous probability term ($\nabla \mathbf{w} = \nabla \mathbf{P}$), allowing the optimizer to adjust physical parameters based on the likelihood of the path taken. Further details on the specific reparameterization functions used for scattering and reflection are provided in Appendix D 1.

With the new trajectory established via the STE, the simulation state is advanced to the next iteration ($k \rightarrow k + 1$). The ray’s global time is incremented by the flight time over the selected path length. Simultaneously, the survival factor α , which tracks the fraction of the ray’s intensity that has not been absorbed or detected, is updated to account for the attenuation along the new path. This recursive cycle of intersection, deposition, and state update continues for a fixed number of iterations K . The value of K is chosen to ensure that the unsimulated residual intensity is negligible; convergence studies justifying this choice are presented in Appendix D 3. For

FIG. 6. **(Left)** Geometric definition of the photon relaxation model. A photon with Gaussian width σ passes a sensor of radius r at an impact parameter b . The purple shaded region illustrates the integral of the photon’s probability density over the sensor surface, which determines the weight w_{geo} assigned to the hit. **(Right)** The calculated overlap probability w_{geo} as a function of the normalized impact parameter b/r . As the smoothing width σ increases, the response transitions from a non-differentiable step function (binary) to a smooth curve that provides useful gradients even when the ray strictly misses the sensor ($b/r > 1$).



a complete description of the logic flow and pseudocode, we refer the reader to the detailed propagation algorithm in Appendix D.

E. Hit Making

The final step converts the predicted rays arriving at each sensor into continuous, differentiable observables. In this work, we focus primarily on the expected photoelectron counts, commonly referred to as *charge*, which constitute the main input to the calibration and reconstruction studies presented in Secs. III and IV.

The expected charge at sensor j is defined as the sum of the ray intensities deposited across all propagation steps, scaled by the wavelength-averaged sensor quantum efficiency (QE)^{vii}:

$$Q_j = \text{QE} \sum_{(i,k) \in \mathcal{H}_j} n_{\text{dep},i,k}, \quad (17)$$

where \mathcal{H}_j denotes the set of all ray–step pairs (i, k) that intersect sensor j , and $n_{\text{dep},i,k}$ is the fractional photon count deposited by ray i during propagation step k .

In addition to charge, the framework naturally provides differentiable expectations for photon arrival times.

We define a smooth approximation to the earliest-arrival time at sensor j as

$$t_j^{\text{soft}} = t_j^{\text{min}} - T \log \left(\sum_{i \in j} e^{-(t_i - t_j^{\text{min}})/T} \right), \quad (18)$$

where t_j^{min} is the minimum arrival time among all rays reaching sensor j , and T is a temperature parameter controlling the smoothness of the approximation while preserving differentiability.

While charge predictions converge to the true expectation as the number of sampling rays increases, the same is not true for this hit-level time estimator. As the number of rays grows, the soft-minimum time converges to the earliest *geometrically allowed* arrival time, corresponding to the direct time of flight from the emission point to the photosensor. This quantity is well known analytically and does not correspond to the experimentally observed first-photon time, which depends on stochastic photon statistics and the sensor response.

For this reason, we do not directly use the hit-level time expectation in the main reconstruction pipeline. Instead, timing information is incorporated through time-of-flight residuals defined with respect to this analytic earliest-arrival proxy when constructing the reconstruction losses in Sec. IIH. This approach provides stable and informative gradients while remaining robust against variations in the number of sampling rays.

A fully consistent use of time information at the hit-making level would require extending the present hit-centered paradigm to a waveform-based differentiable expectation, in which the full temporal response converges with increasing sampling statistics. Such an extension would require additional modeling choices, includ-

^{vii} The wavelength-averaged QE for the SK-like detector corresponds to 6.5%. This value is obtained by folding the wavelength-dependent quantum efficiency of the Super-Kamiokande photomultipliers (Hamamatsu PMT R3600 [41]) with the average photon wavelength distribution for 1 GeV muon events in water as predicted by GEANT4.

ing explicit assumptions about sensor response functions. While fully compatible with the present framework, this refinement is beyond the scope of this work, particularly since the hit-based approach already achieves state-of-the-art reconstruction performance, as demonstrated in Sec. IV.

F. Performance

A key practical requirement for end-to-end differentiable simulation is that gradient evaluation must not introduce prohibitive overhead. In LUCiD, the dominant cost is ray propagation, which scales with the total number of ray–step updates, i.e. approximately $O(N_{\text{rays}} \times K)$, where N_{rays} is the number of simulated rays and K is the maximum number of propagation iterations. Figure 7 quantifies this scaling in an SK-like geometry using a single NVIDIA A100 GPU for two modes: (i) forward prediction of expected hit patterns (“Prediction Only”), and (ii) forward prediction together with reverse-mode automatic differentiation to compute gradients with respect to the chosen parameters (“Prediction and Gradient Calculation”).

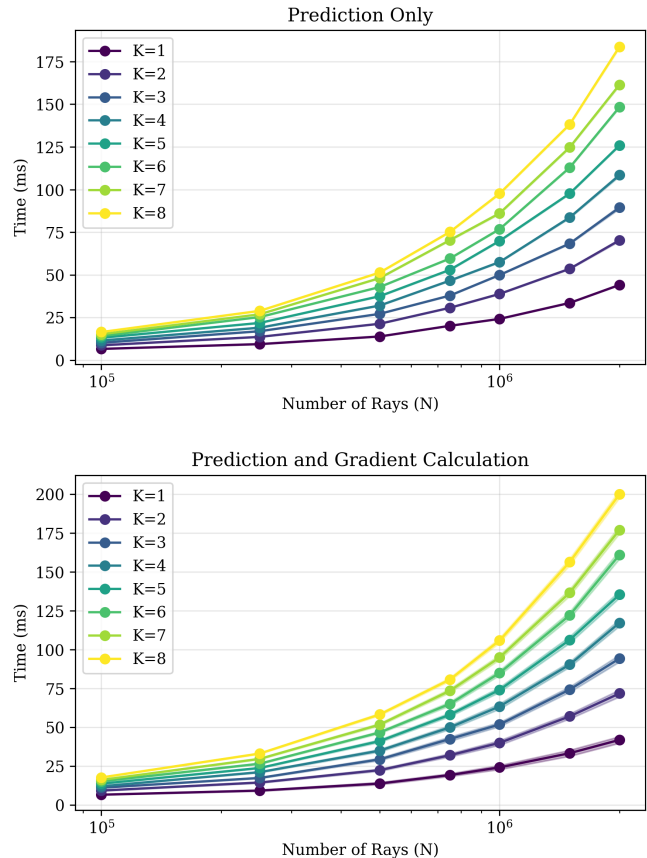
Across the full scanned range, the runtime increases smoothly with both N_{rays} and K , consistent with the expected linear dependence on the number of ray–surface interactions. For representative configurations used elsewhere in this work (e.g. $K = 8$ and $N_{\text{rays}} \sim 10^5$ prediction-only executions are $\mathcal{O}(10)$ ms.

Increasing the propagation depth from $K = 1$ to $K = 8$ yields an approximately proportional increase in runtime, indicating that the per-step propagation logic (intersection lookup, weighting, and state update) dominates the computational cost.

Crucially, enabling gradient evaluation adds only a modest, near-constant multiplicative overhead relative to the forward pass of ~ 10 – 15% over the full N_{rays} range in Fig. 7. This behavior is a direct consequence of reverse-mode AD: once the forward computation graph is constructed, the cost of obtaining all derivatives of a scalar loss with respect to a (potentially large) parameter vector is roughly a constant factor times the forward cost, rather than scaling linearly with the number of optimized parameters. This property is essential for the calibration results in Sec. III, where we optimize thousands of sensor parameters simultaneously, and for tracking in Sec. IV, where all the particle track degrees of freedom are updated jointly.

Taken together, these timing results demonstrate that LUCiD supports gradient-based calibration and reconstruction at essentially the same computational scale as forward simulation, with runtime controlled primarily by user-chosen accuracy knobs (N_{rays} , K) rather than by the dimensionality of the inference problem.

FIG. 7. Computation time for hit prediction and gradient evaluation in an SK-like detector geometry, shown as a function of the number of rays (N) and the number of propagation iterations (K). The line thickness indicates the time uncertainty.



G. Generating Data-like Events

To validate and benchmark the differentiable simulation, we generate *data-like* events, i.e., fully stochastic realizations that reproduce the statistical characteristics of real detector data for a given geometry and configuration. These events serve as reference samples against which to compare the differentiable, expectation-based predictions described in previous sections.

Conceptually, *data-like* events are produced by switching from the expectation-weighted, differentiable estimation with continuous weights and smooth hit formation to a photon-level Monte Carlo mode.

- **Light generation:** Instead of using the trained SIREN surrogate for photon emission, we directly inject event-by-event information from PHOTON-SIM, corresponding to GEANT4-generated photon-by-photon predictions such as those earlier shown in Figure 2. This approach ensures that the microscopic emission processes are fully sampled rather than represented through an averaged, differen-

tiable surrogate.

- **Propagation:** The photon propagation stage follows the same effects described in Sec. IID, but all probabilistic interactions are now sampled explicitly for each photon instead of being represented through continuous weights, and Gaussian relaxation is disabled. Each photon evolves independently according to its randomly determined trajectory, thereby reproducing the inherent stochasticity of photon transport in the detector medium.
- **Hit formation:** In the *data-like* mode, all photons carry unit weight and contribute discretely to the hit pattern. The hit-making process mirrors that of real detector data: each photon is either detected or not, according to the sensor’s quantum efficiency, and the hit time is computed directly from the arrival time of the first detected photon without any soft-minimum approximation. Random smearing is applied to both the hit times and charges to reproduce the detector resolution. By default, the amount of smearing matches the performance of the Super-Kamiokande detector as reported in Ref. [42]. Specifically, hit times are Gaussian-smearred by 0.4 ns, and the observed charge is smeared by 1.2% for fewer than 20 counts, 0.75% for up to 130 counts, and 0.5% for larger signals. Additionally, we introduce a random shift to all event times adding a random uniform t_0 value to all hits in a ± 20 ns window, much larger than the t_0 reconstruction resolutions reported later.

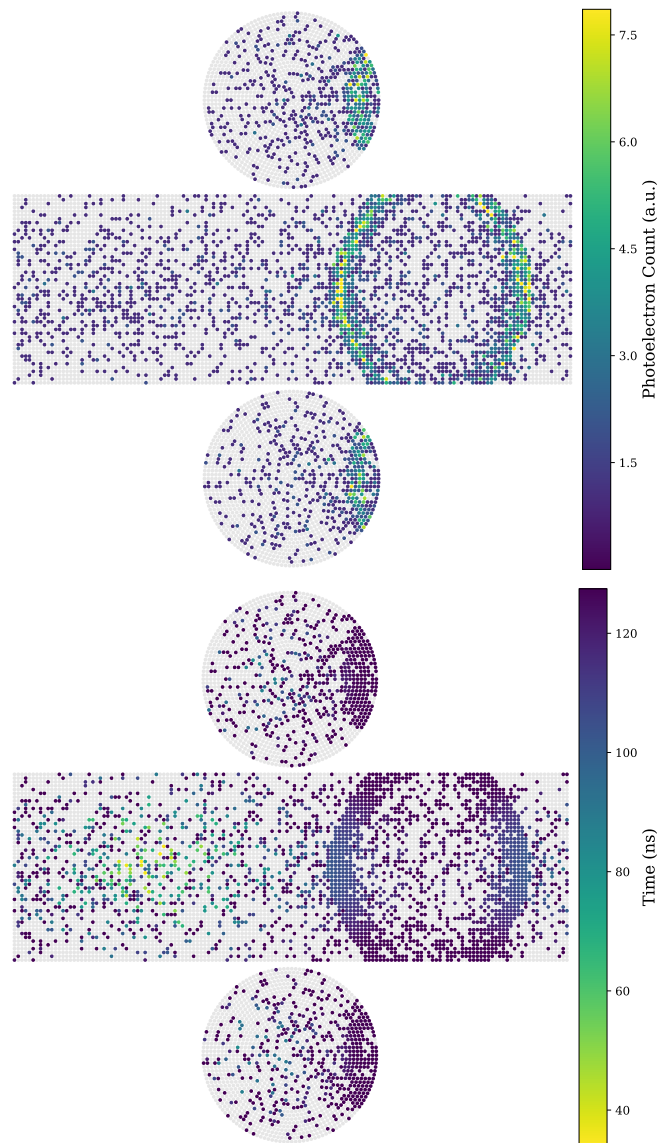
Figure 8 shows corresponding charge and time expectations for the same data-like event in the SK-like detector.

We illustrate this pipeline working in multiple geometries in Figure 9, where side-by-side comparisons of *data-like* events and their corresponding differentiable expectations, generated with identical particle and detector configurations across multiple geometries.

H. Losses

To illustrate gradient-based calibration and optimization, we employ the loss functions described below. Our aim is to demonstrate the capabilities of the differentiable framework rather than to optimize the loss design itself. Accordingly, the performance results presented in subsequent sections should be interpreted as baseline performance estimates that could be further improved through dedicated loss-function development.

FIG. 8. Example of a 1 GeV muon data-like event in the SK-like detector. Dark noise is not included.



1. Tracking

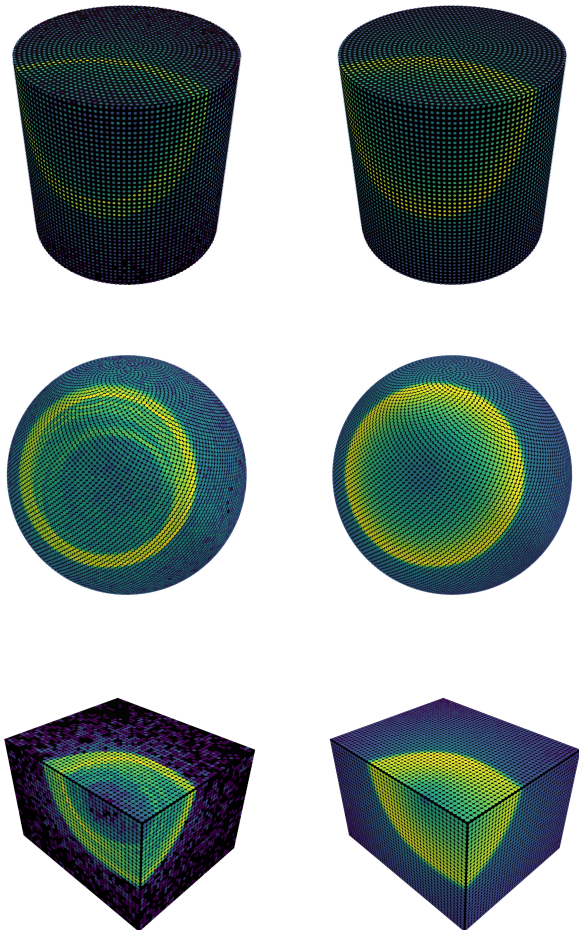
Track reconstruction is formulated through a composite loss,

$$\mathcal{L}_{\text{tracking}} = \sqrt{(\mathcal{L}_{\text{vertex}} + \epsilon) (\mathcal{L}_{\text{counts}} + \epsilon) (\mathcal{L}_{\text{cone}} + \epsilon)}, \quad (19)$$

where $\epsilon = 10^{-6}$ prevents vanishing gradients. The geometric mean avoids additional weighting hyperparameters while requiring simultaneous improvement of all components, ensuring balanced contributions from vertex timing, charge, and cone timing terms.

For a hypothesized vertex \mathbf{x}_0 , track angles (θ, ϕ) , and energy E , the count term is defined as the normalized

FIG. 9. Example data-like events and associated differentiable predictions for various detector geometries. The color intensity represents the observed counts in logarithmic scale.



Poisson negative log-likelihood:

$$\mathcal{L}_{\text{counts}} = \frac{\sum_i (\hat{n}_i - n_i \log(\hat{n}_i + \epsilon) + \log \Gamma(n_i + 1))}{\sum_i n_i + \epsilon}, \quad (20)$$

where n_i and \hat{n}_i denote observed and predicted photoelectron counts for photosensor i . The $\log \Gamma(n_i + 1)$ term ensures correspondence with the full Poisson likelihood, although it does not contribute to gradients. The normalization reduces event-to-event scale variations and promotes agreement of the predicted and observed charge patterns across the detector.

The time-based components employ a smooth pinball (quantile) loss,

$$\rho_\tau(r; \sigma) = \tau \text{softplus}(r/\sigma) \sigma + (1 - \tau) \text{softplus}(-r/\sigma) \sigma, \quad (21)$$

with $\text{softplus}(x) = \log(1 + e^{-|x|}) + \max(x, 0)$. Here $\tau \in (0, 1)$ specifies the quantile and σ controls smoothness. The loss is minimized when the τ -quantile of the residual distribution vanishes and is well suited to asym-

metric residual distributions with extended tails, providing robustness while remaining fully differentiable.

For a vertex hypothesis \mathbf{x}_0 and start time t_0 , the earliest photon arrival time at photosensor i is

$$t_i^{\text{exp}} = \frac{\|\mathbf{x}_i - \mathbf{x}_0\| - r_s}{c_{\text{med}}}, \quad (22)$$

where \mathbf{x}_i is the detector position, r_s the photosensor radius, and c_{med} the speed of light in the medium. The vertex timing loss is constructed from residuals $\Delta t_i^{\text{vertex}} = t_i^{\text{obs}} - t_i^{\text{exp}} - t_0$,

$$\mathcal{L}_{\text{vertex}} = \frac{\sum_i w_i \rho_{\tau_v}(\Delta t_i^{\text{vertex}}; \sigma_v)}{\sum_i w_i + \epsilon}, \quad (23)$$

with $w_i = 1$ for photosensors with observed charge $q_i > 0$ and zero otherwise, $\tau_v = 0.23$, and $\sigma_v = 0.25$ ns. Binary weighting avoids biasing the earliest-light estimate toward high-charge sensors.

The cone timing term compares observed hit times to predicted arrival times \hat{t}_i from the full simulation,

$$\mathcal{L}_{\text{cone}} = \frac{\sum_i q_i \rho_{\tau_c}(\Delta t_i^{\text{cone}}; \sigma_c)}{\sum_i q_i + \epsilon}, \quad (24)$$

where $\Delta t_i^{\text{cone}} = t_i^{\text{obs}} - \hat{t}_i - t_0$, $\tau_c = 0.12$, and $\sigma_c = 0.25$ ns. In contrast to the vertex term, charge weighting incorporates information from the Cherenkov light pattern.

The hyper-parameters τ_v and τ_c were selected studying the 1D loss landscape of t_0 and the vertex position.

III. CALIBRATION

Calibration serves to ground the simulation in physical reality, ensuring that the digital model faithfully reproduces the behavior of the actual detector. By aligning the tunable parameters θ_{detector} with control data, we establish a baseline for all subsequent analyses. In our differentiable framework, this process is formulated as a gradient-based optimization where we minimize the negative log-likelihood of the observed photoelectron counts, $\mathcal{L}_{\text{counts}}$ (Eq. 20).

We present two distinct calibration campaigns: tuning the optical properties of the detector using a central laser source, and characterizing individual sensor efficiencies using distributed isotropic sources.

A. Methodology and Variance Reduction

Calibration requires high sensitivity to parameter changes. Unlike the tracking stage, which utilizes the photon relaxation model for smoother position and direction gradients (to be discussed in Sec. IV), here we rely on the strict Monte Carlo nature of binary ray-sensor intersections to capture the exact geometric acceptance. While this accuracy is essential, it introduces stochastic

noise into the gradients. To mitigate variance and ensure stable convergence without artificially removing noise, we employ two targeted strategies.

First, to ensure isotropic coverage with minimal sampling variance in the forward model, we generate photon trajectories using the deterministic Fibonacci lattice described in Sec. II C. The reference data against which predictions are compared is instead produced using pseudo-random sampling. This separation ensures that the optimization gradients are driven by sensitivity to physical parameters rather than stochastic noise from non-uniform sampling.

Second, we address the sparsity of the light patterns produced by calibration sources. In the laser configuration, sensors not aligned with the primary photon beam only detect light resulting from scattering or reflection. These low-statistic contributions can lead to vanishing or noisy gradients. To prevent this, we implement a smoothed loss calculation: both the simulated and reference hit patterns are convolved with a Gaussian kernel ($\sigma = 50$ cm) before evaluating $\mathcal{L}_{\text{counts}}$. This relaxation effectively spreads the signal influence, allowing gradients to flow from the sparse regions even during the early stages of optimization when the data-simulation mismatch is large.

Optimization is performed using the Adam optimizer [43]. For the laser calibration specifically, we employ a learning rate warmup schedule to further stabilize the trajectory against large initial gradients.

B. Detector Property Extraction

We first address the optical properties of the detector: the Rayleigh scattering length λ_s , absorption length λ_a , wall reflection rate R_w , and sensor reflection rate R_s . Accurately determining these values is challenging due to the strong correlations between them; for instance, increasing scattering or absorption both result in light attenuation.

We simulated a central laser source positioned at the center of the top end-cap and oriented vertically downward, and performed simultaneous optimization of these four parameters over 500 training iterations. To test the robustness of the method against local minima, we launched the optimization from multiple different initial parameter guesses for the same true configuration.

Figure 10 (Left) illustrates the trajectories of the parameters. Despite the varying starting points, the gradients, derived from the smoothed charge distribution, successfully guide all independent runs toward the true physical values. This confirms that the differentiable simulation can disentangle correlated effects by leveraging the full spatial information of the hit patterns, not just the total charge. Figure 10 (Right) visualizes the loss landscape for scattering versus absorption, showing a clear global minimum that the optimizer navigates effectively.

C. Sensor Efficiency Calibration

The second study focuses on the QE of individual photosensors. Calibrating N_{sensors} independent parameters ($\sim 10^4$ in this geometry) is traditionally a computationally intensive task.

We modeled this calibration using 15 isotropic light sources: one central source and 14 distributed in a grid pattern ($x, y, z \in \{0, \pm 10\text{m}\}$) throughout the volume. The global detection efficiency scale is absorbed into the per-sensor corrections, removing the need for a separate normalization parameter. Because the isotropic illumination provides broad coverage compared to the laser, $\mathcal{L}_{\text{counts}}$ is computed directly without additional smoothing.

Initialized with a uniform efficiency assumption, the optimizer utilizes gradients accumulated from all 15 source positions to break geometric degeneracies. Figure 11 demonstrates the convergence of the sensor parameters. The residuals between the fitted and true QE values narrow rapidly, confirming that LUCiD can successfully recover fine-grained detector calibrations in a high-dimensional parameter space.

IV. TRACKING

The differentiable simulator developed in the previous sections enables gradient-based reconstruction of particle tracks. Given a set of observed detector hits, we optimize the event parameters to identify the track hypothesis that best explains the data. Inference is performed using the Adam optimizer [43], applied directly to the physical track parameters: vertex position \mathbf{x} , emission time t_0 , direction $\boldsymbol{\omega} = (\theta, \phi)$, and energy E . To ensure stable convergence across parameters with different physical scales^{viii}, we employ parameter-specific learning rates of (0.25, 0.5, 0.025, 50.0) for $(\mathbf{x}, t_0, \boldsymbol{\omega}, E)$, respectively, with standard Adam settings $(\beta_1, \beta_2) = (0.9, 0.999)$. The optimization updates all seven degrees of freedom simultaneously over a user-defined number of iterations. All tracking studies use a fixed scattering length of 50 m, a wall and sensor reflection of 20%, and an absorption length of 50 m, well-aligned with SK [42].

Figure 12 illustrates the optimization trajectories for a representative data-like event, projected onto several two-dimensional parameter slices. Each trajectory corresponds to a different random initialization of the track parameters. Regardless of the starting point, the optimizer consistently converges to the correct solution

^{viii} Reasonable parameter scales were determined heuristically by searching for parameter combinations that reduced the average parameter errors at a similar rate. While sensible scales reduce the necessary iterations for convergence, we observed that a wide range of scaling values ensured consistent convergence to the global minimum.

FIG. 10. (Left) Convergence of medium parameters ($\lambda_s, \lambda_a, R_w, R_s$) from multiple random initializations. All trajectories converge to the true values (dashed lines). (Right) The 2D loss landscape for scattering versus absorption length. The gradients (white arrows) drive the parameters through the correlated valley toward the true minimum (red star).

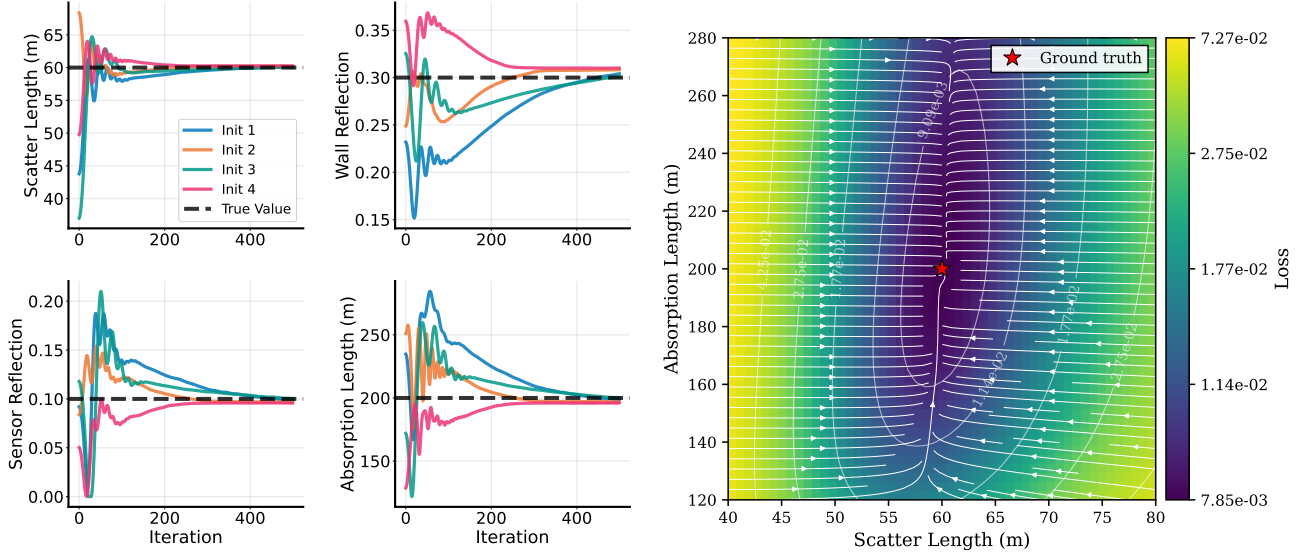
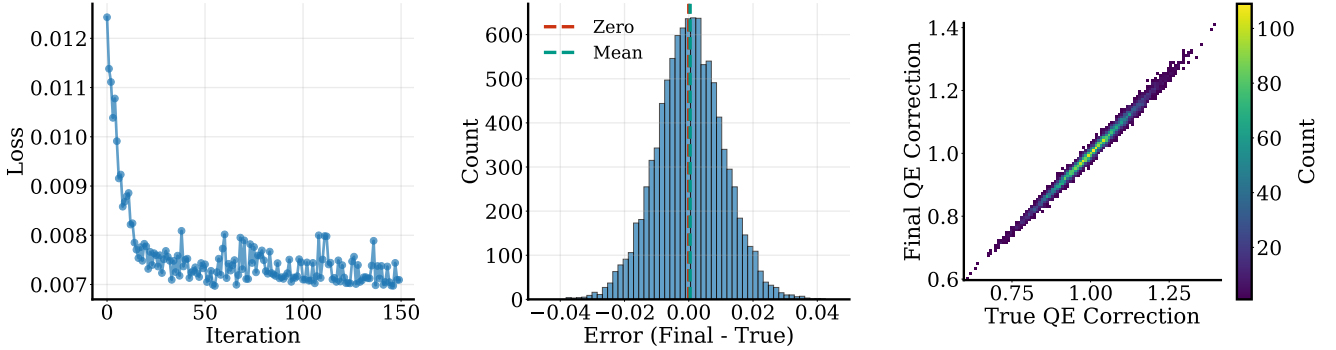


FIG. 11. Per-sensor quantum efficiency (QE) corrections. The loss function converges rapidly within the first ~ 50 iterations as the optimization cycles through multiple calibration source positions. The final residual distribution (predicted $-$ true QE correction) is centered near zero with an RMS of 1.0%, demonstrating unbiased prediction.



through gradient-based minimization. Convergence is typically achieved even for initial conditions far from the true values, except in cases where the predicted light reflection pattern closely resembles the true event topology. In such cases, the optimizer may settle in a local minimum. These ambiguities are easily mitigated by performing a coarse grid search over the initial parameter space, as detailed in Appendix E.

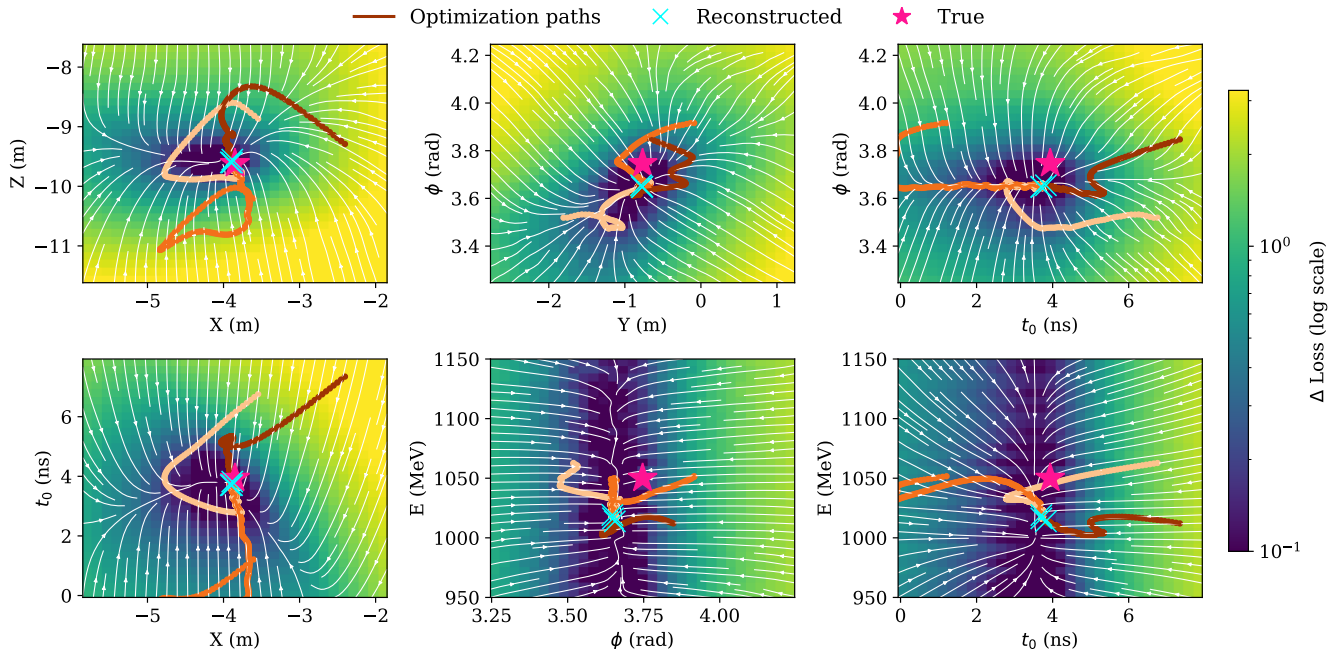
For quantitative performance studies, we reconstruct 500 muon events with $E_\mu = 1050$ MeV (approximately 1 GeV visible energy) simulated in the SK-like detector. Events are required to have both the track origin and end contained within 90% of the inner detector volume to match standard fiducial volume requirements. Data-like samples are produced with $K = 20$ to ensure that high-order effects are fully included. The expectation is evaluated with $K = 7$, which is sufficient since further

increasing K results in negligible changes to the predictions.

Figure 13 shows the convergence behavior of the position, direction, t_0 , and momentum errors as a function of optimization iteration. For $N_{\text{rays}} \sim 50\text{k}$, the performance reaches convergence, corresponding to a total runtime of ~ 15 seconds per event for 300 optimization iterations. In practice, approximately 100 iterations are sufficient for stable convergence. Thus, further speed improvements might be possible implementing early stopping, resulting in single particle reconstruction times well below 10 seconds, comparable to state-of-the-art alternatives.

The reconstruction performance as a function of N_{rays} is summarized in Fig. 14. We obtain a vertex resolution of approximately 15.6 cm, an angular resolution of 1.1° , and a momentum resolution of 1.5%. These results are comparable to those achieved by FitQun (15.8 cm,

FIG. 12. Two-dimensional loss landscape for different parameter combinations, with associated gradient streamlines, as observed in a randomly selected data-like event. The true parameter values are indicated by red stars.



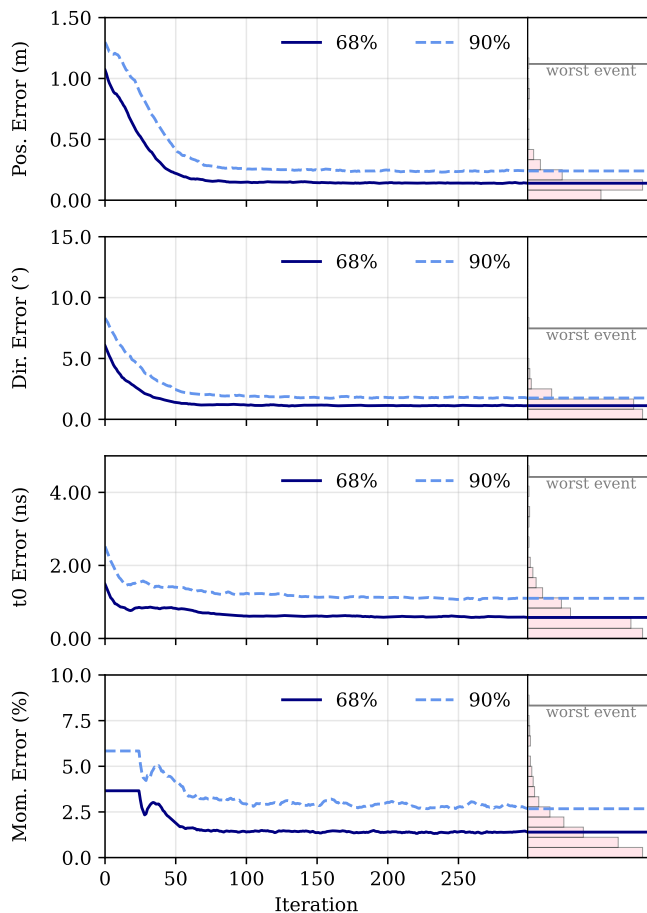
1.0° , 2.3%), when evaluated on a similar simulated data set [36]. While this comparison should be interpreted qualitatively, since our detector geometry, sensor response, and medium properties do not exactly replicate those of Super-Kamiokande, the close agreement demonstrates that the proposed differentiable approach can reach performance levels comparable to state-of-the-art, non-differentiable methods. At the same time, it offers improved computational efficiency, calibration capabilities and the additional benefits discussed in the introduction. Moreover, the error distributions remain consistently narrow across all tested events, with no observed reconstruction failures and only small tails. These tails are comparable to those observed in FitQun [44] and are consistent with unlikely data-like events, such as large early scattering of the muon that are not well represented by the average prediction. This indicates stable optimization behavior and suggests that the approximations introduced in LUCiD do not lead to any appreciable degradation of the reconstruction performance when compared to FitQun.

The performances of the track reconstruction vary smoothly with the simulated track energy, see Figure 15, and demonstrates that the simulator already performs well across a wide range of energies. Small residual fluctuations in the momentum resolution suggest minor imperfections in the surrogate Cherenkov light-emission model, which could be further refined in future work. Nevertheless, the worst observed momentum resolution of about 2% is already excellent.

V. APPLICATION TO DETECTOR DESIGN

A persistent challenge in detector design optimization is that the key performance metrics are typically reconstruction metrics, such as those presented in the previous section, yet reconstruction algorithms are often tuned to a given detector geometry. Adapting them to alternative designs is therefore a labor- and compute-intensive task. For example, FitQun avoids explicit ray tracing by relying on parametrizations derived from sensor-by-sensor lookup tables. A limitation of this approach is that these tables and parametrizations are valid only for a fixed geometry, requiring the entire reconstruction procedure to be re-tuned and re-validated whenever the detector design changes. In contrast, our differentiable framework performs ray tracing on the fly for arbitrary detector configurations, enabling direct comparison of reconstruction performance across different geometries without any re-training or re-tuning. This capability makes detector design optimization straightforward: performance metrics can be evaluated consistently for a standard dataset while varying geometry or sensor parameters. Figure 16 illustrates this concept using the same configuration as in Fig. 14, but varying the number of photosensors in the SK-like detector. The same strategy can be generalized to explore multi-dimensional design spaces, for instance by varying sensor detection efficiency, timing and photoelectron resolution, detector size, or shape. This provides a practical pathway to detector design within experimental and budgetary constraints.

FIG. 13. Evolution of reconstruction errors over optimization iterations for the track vertex position, direction, interaction time (t_0), and particle momentum.



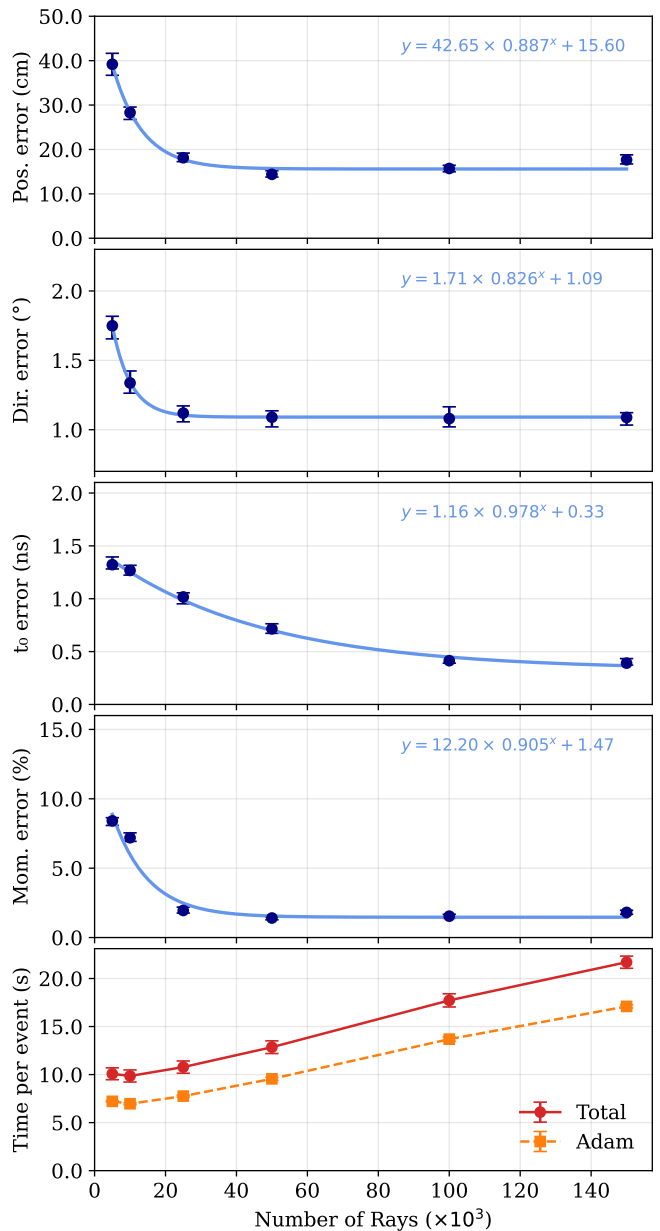
VI. FUTURE DIRECTIONS

A. Complex Topologies

Although multi-particle optimization is left for future work, the losses described above can be naturally extended to events involving multiple simultaneous particles. This requires no conceptual modification of the framework, as the expected charges and times for the full event can be expressed as differentiable combinations of the corresponding quantities from each individual particle. In practice, this simply entails evaluating the hit-making logic for the rays associated with all particles in the event, rather than for a single particle. The gradients obtained through backpropagation will then point in directions that simultaneously improve the reconstructed parameters of all particles, automatically accounting for overlapping light patterns.

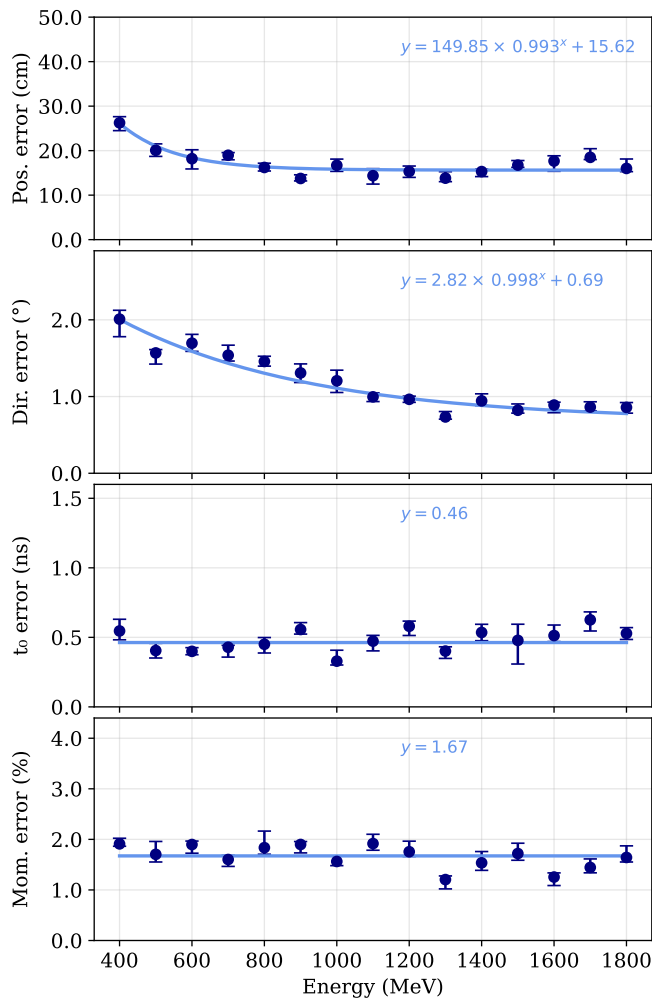
A related extension concerns tracks with hard scatterers, particularly relevant for charged pions undergoing hadronic interactions. Such events can be modeled as multiple connected track segments sharing a com-

FIG. 14. Tracking performance as a function of the number of rays, N_{rays} .



mon vertex at the scattering point, with gradients naturally favoring kink locations that best explain the observed light distribution. Reconstructing such topologies also raises the question of model selection: the simplest approach is to perform reconstruction under several particle-number hypotheses and compare results using likelihood ratios or information criteria. However, gradient information may also inform model selection, by initializing with excess particles whose contributions are suppressed during optimization if not supported by the data.

FIG. 15. Tracking performance as a function of the simulated muon energy.

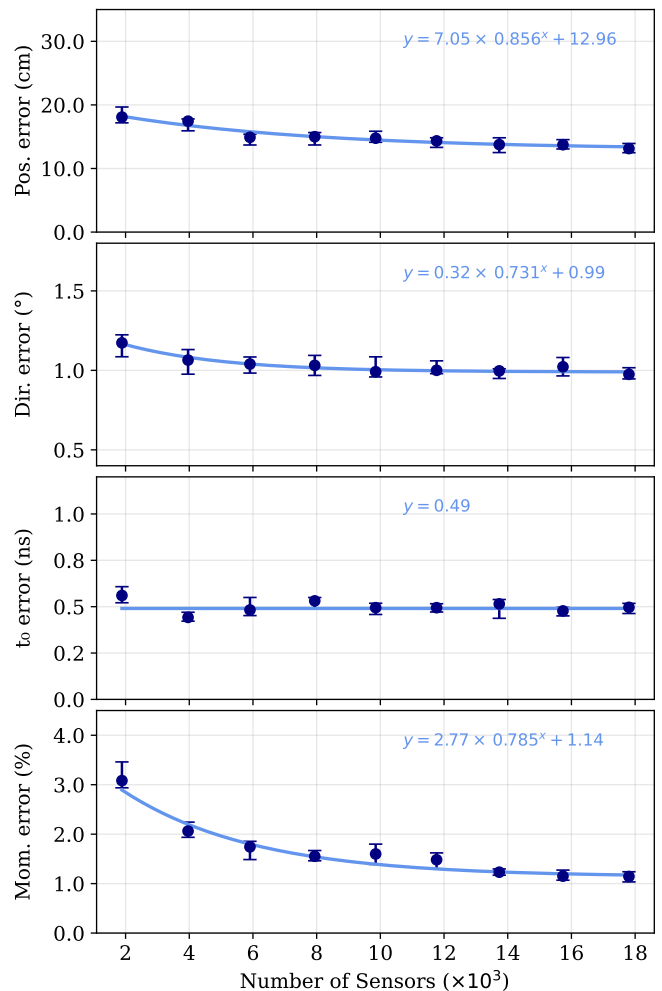


B. Extension to Complex Geometries

The current implementation relies on analytic ray-surface intersection for simple boundary geometries and a two-dimensional grid acceleration structure for sensor lookup. Extending to detectors with volumetric arrays of photosensors, such as neutrino telescopes (e.g., IceCube, KM3NeT), is a natural next step, requiring generalization of the intersection logic and grid mapping to accommodate sensor arrays that are not confined to a single surface.

For detectors with multiple instrumented regions, such as an Inner Detector (ID) surrounded by an Outer Detector (OD) or external cosmic-ray veto systems, modest extensions to the present framework would be sufficient. These could involve either expanding the differentiable geometry to include multiple coupled volumes with distinct optical and sensor properties, or combining the reconstruction of the primary target volume with auxiliary veto information at a separate stage.

FIG. 16. Tracking performance as a function of the number of photosensors.



To accommodate arbitrarily complex detector geometries more generally, a promising approach is to represent surfaces as neural implicit functions, following recent advances in neural radiance fields [45]. Such representations can learn complex shapes from CAD models or calibration data while remaining fully differentiable, enabling gradient-based optimization without requiring analytic intersection formulas for each component. This would also allow modeling of realistic, non-spherical, PMT geometries, which affect both acceptance and timing response.

This flexibility comes with a tradeoff: detailed geometric representations require additional intersection evaluations, increasing computational cost. Balancing geometric fidelity against reconstruction speed will be an important consideration for applying this framework to detectors with complex optical module designs, multi-region instrumentation, or irregular layouts.

C. Extended Detector Modeling

The current implementation treats photosensors as ideal spherical surfaces and produces hit-level observables. Extending to waveform-level predictions requires addressing the discontinuity of time binning, which can be achieved through kernel density estimation to maintain differentiability. This would enable more sophisticated timing estimators that extract information directly from waveform features.

Real PMTs exhibit complex quantum efficiency and photoelectron transit time profiles that depend on the photon incident position and direction. The modular architecture of the framework naturally accommodates learning the PMT response maps as a function of multiple variables from laboratory measurements or detailed simulations using a network architecture similar to the SIREN employed for Cherenkov emission (Sec. II C). Once trained, this component integrates directly after the photon ray tracing in the PMT hit making step. For modules housing multiple PMTs, as those to be used in Hyper-Kamiokande and IceCube, the same approach extends to learning a response map that distributes an incident photon’s contribution across the constituent sensors based on where it strikes the outer enclosure.

This modularity enables a practical two-stage calibration strategy. First, a base PMT response map is trained from laboratory characterization of a reference sensor, capturing the intrinsic response shared by all units of the same type. Then, during in-situ calibration, the full PMT response map for each installed sensor can be refined using calibration sources rather than being limited to simple scaling as in conventional approaches. The differentiable framework makes this higher-dimensional optimization tractable.

Real detector media exhibit spatial variations in optical properties due to impurities, temperature gradients, or material aging effects. These inhomogeneities affect light propagation and visibility but are difficult to model beyond simple parameterizations. A SIREN-like network can represent spatially and temporally varying scattering and absorption lengths as continuous fields, with rays sampled volumetrically to compute path-dependent attenuation. Such a model could be learned directly from calibration data, capturing detector inhomogeneities and their evolution over time.

D. Stochastic Extensions

The simulation operates in expected-value mode throughout, propagating intensity-weighted rays rather than sampling individual photon fates. However, certain processes exhibit irreducible stochasticity that may be important to capture. Examples include the distribution of outcomes when photons undergo multiple internal reflections within a photosensor assembly, and particle-level fluctuations, such as electromagnetic showering, in

light emission.

Generative models such as normalizing flows [46] provide a natural framework for differentiable stochastic simulation. These approaches structure the random sampling process in a way that allows gradients to propagate through, enabling end-to-end training against detector data. This would allow learning physical fluctuation distributions directly from observation rather than relying solely on first-principles simulation.

E. Towards End-to-End Differentiable Analysis

Beyond unifying traditionally fragmented workflows, the differentiable framework enables capabilities that were previously impractical. Automatic differentiation provides not only gradients but also efficient Hessian computation, giving access to curvature information for uncertainty estimation. This allows calibration uncertainties to propagate through reconstruction into physics results while preserving correlations, whereas current approaches typically lose information at each stage boundary.

The differentiable detector simulation presented here forms one component of a potentially fully differentiable analysis chain. Upstream, this could connect to differentiable event generation and interaction physics, propagating gradients from theory parameters through particle production into detector response. Downstream, extension to differentiable likelihood construction and sensitivity metrics would enable optimization from detector configuration through to physics results. Such a complete pipeline would allow gradients to flow from fundamental physics parameters to final measurements.

Finally, the modular architecture facilitates extension to detectors with multiple readout modalities. Liquid argon time projection chambers, for example, provide both scintillation light and ionization charge. Differentiable simulations developed independently for each modality can be composed within a unified framework, enabling joint reconstruction and co-optimization of how information from each readout is combined.

VII. CONCLUSIONS

In conclusion, we have introduced LUCiD, the first end-to-end differentiable simulation framework for large-scale homogeneous optical particle detectors that unifies light generation, propagation, and sensor response within a single gradient-based optimization pipeline. By targeting smooth, differentiable expectations in detector-output space while retaining high-fidelity validation through a complementary data-like Monte Carlo mode, LUCiD enables calibration and reconstruction to be performed simultaneously and efficiently. This directly challenges the long-standing state-of-the-art approach

in experimental particle physics, which relies on non-differentiable sampling-based simulators for simulation, calibration and reconstruction procedures.

We demonstrated that physically meaningful and stable gradients can be obtained across all key stages of optical detector response, including light emission, transport, medium interactions, boundary reflections, and sensor acceptance. These capabilities enable robust gradient-based extraction of correlated medium parameters, high-dimensional per-sensor efficiency calibration at the scale of tens of thousands of parameters, and competitive track reconstruction performance in an SK-like detector geometry. In all cases, the differentiable approach matches or surpasses conventional methods in accuracy while offering a simpler, more unified, and computationally efficient workflow.

Taken together, these results constitute the first demonstration that end-to-end differentiable simulation is not only viable but practically ready for use in ongoing and future optical detector experiments. By removing artificial boundaries between simulation, calibration, and reconstruction, this work provides the essential in-

redients for a paradigm shift in how detector modeling and data analysis are performed in particle physics, opening the door to fully integrated optimization, uncertainty propagation, and detector design within a single coherent framework.

ACKNOWLEDGMENTS

We acknowledge valuable discussions within the CIDEr-ML collaboration, especially with K.M. Tsui, M. Wilking, and J. Xia, on conventional simulation and water Cherenkov detector modeling. This work was supported by the Center for Data-Driven Discovery, Kavli IPMU (WPI), JSPS KAKENHI Grant Number JP24K23938, the Ozaki Exchange Program, the U.S. Department of Energy, Office of Science, Office of High Energy Physics, and U.S.-Japan Science and Technology Cooperation Program under Contract DE-AC02-76SF00515.

-
- [1] Y. Fukuda *et al.* (Super-Kamiokande), *Nucl. Instrum. Meth. A* **501**, 418 (2003).
- [2] J. Boger *et al.* (SNO), *Nucl. Instrum. Meth. A* **449**, 172 (2000), [arXiv:nucl-ex/9910016](#).
- [3] A. Piepke (KamLAND), *Nucl. Phys. B Proc. Suppl.* **91**, 99 (2001).
- [4] G. Alimonti *et al.* (Borexino), *Nucl. Instrum. Meth. A* **600**, 568 (2009), [arXiv:0806.2400 \[physics.ins-det\]](#).
- [5] F. P. An *et al.* (Daya Bay), *Nucl. Instrum. Meth. A* **811**, 133 (2016), [arXiv:1508.03943 \[physics.ins-det\]](#).
- [6] M. G. Aartsen *et al.* (IceCube), *JINST* **12**, P03012 (2017), [Erratum: *JINST* **19**, E05001 (2024)], [arXiv:1612.05093 \[astro-ph.IM\]](#).
- [7] S. Adrian-Martinez *et al.* (KM3Net), *J. Phys. G* **43**, 084001 (2016), [arXiv:1601.07459 \[astro-ph.IM\]](#).
- [8] F. An *et al.* (JUNO), *J. Phys. G* **43**, 030401 (2016), [arXiv:1507.05613 \[physics.ins-det\]](#).
- [9] K. Hirata *et al.* (Kamiokande-II), *Phys. Rev. Lett.* **58**, 1490 (1987).
- [10] Y. Fukuda *et al.* (Super-Kamiokande), *Phys. Rev. Lett.* **81**, 1562 (1998), [arXiv:hep-ex/9807003](#).
- [11] S. Fukuda *et al.* (Super-Kamiokande), *Phys. Rev. Lett.* **86**, 5651 (2001), [arXiv:hep-ex/0103032](#).
- [12] Q. R. Ahmad *et al.* (SNO), *Phys. Rev. Lett.* **89**, 011301 (2002), [arXiv:nucl-ex/0204008](#).
- [13] Q. R. Ahmad *et al.* (SNO), *Phys. Rev. Lett.* **87**, 071301 (2001), [arXiv:nucl-ex/0106015](#).
- [14] K. Eguchi *et al.* (KamLAND), *Phys. Rev. Lett.* **90**, 021802 (2003), [arXiv:hep-ex/0212021](#).
- [15] T. Araki *et al.* (KamLAND), *Phys. Rev. Lett.* **94**, 081801 (2005), [arXiv:hep-ex/0406035](#).
- [16] F. P. An *et al.* (Daya Bay), *Phys. Rev. Lett.* **108**, 171803 (2012), [arXiv:1203.1669 \[hep-ex\]](#).
- [17] G. Bellini *et al.* (BOREXINO), *Nature* **512**, 383 (2014).
- [18] M. Agostini *et al.* (BOREXINO), *Nature* **587**, 577 (2020), [arXiv:2006.15115 \[hep-ex\]](#).
- [19] G. Bellini *et al.* (Borexino), *Phys. Lett. B* **687**, 299 (2010), [arXiv:1003.0284 \[hep-ex\]](#).
- [20] K. Abe *et al.* (T2K), *Phys. Rev. Lett.* **107**, 041801 (2011), [arXiv:1106.2822 \[hep-ex\]](#).
- [21] K. Abe *et al.* (T2K), *Nature* **580**, 339 (2020), [Erratum: *Nature* **583**, E16 (2020)], [arXiv:1910.03887 \[hep-ex\]](#).
- [22] M. G. Aartsen *et al.* (IceCube), *Science* **342**, 1242856 (2013), [arXiv:1311.5238 \[astro-ph.HE\]](#).
- [23] M. G. Aartsen *et al.* (IceCube), *Science* **361**, 147 (2018), [arXiv:1807.08794 \[astro-ph.HE\]](#).
- [24] S. Aiello *et al.* (KM3NeT), *Nature* **638**, 376 (2025), [Erratum: *Nature* **640**, E3 (2025)].
- [25] A. Abusleme *et al.* (JUNO), (2025), [arXiv:2511.14593 \[hep-ex\]](#).
- [26] I. Esteban, M. C. Gonzalez-Garcia, M. Maltoni, I. Martinez-Soler, J. P. Pinheiro, and T. Schwetz, *JHEP* **12**, 216 (2024), [arXiv:2410.05380 \[hep-ph\]](#).
- [27] K. Abe *et al.* (Hyper-Kamiokande), (2018), [arXiv:1805.04163 \[physics.ins-det\]](#).
- [28] N. Fiza, S. Kim, E. Masaku, M. Masud, H. Nam, J. Park, Y. Park, and K. Siyeon, (2025), [arXiv:2507.07476 \[hep-ph\]](#).
- [29] S. Agostinelli *et al.* (GEANT4), *Nucl. Instrum. Meth. A* **506**, 250 (2003).
- [30] A. G. Baydin, B. A. Pearlmutter, A. A. Radul, and J. M. Siskind, *Journal of Machine Learning Research* **18**, 1 (2018).
- [31] T. Dorigo *et al.*, *Reviews in Physics* **10**, 100085 (2023).
- [32] L. Heinrich and M. Kagan, *Journal of Physics: Conference Series* **2438**, 012137 (2023).
- [33] S. Macaluso, K. Cranmer, and L. Heinrich, *EPJ Web of Conferences* **251**, 03059 (2021).
- [34] N. Simpson and L. Heinrich, *Journal of Physics: Conference Series* **2438**, 012105 (2023).

- [35] S. Gasirowski, Y. Chen, Y. Nashed, P. Granger, C. Mironov, D. Ratner, K. Terao, and K. V. Tsang, *Machine Learning: Science and Technology* **5**, 015045 (2024).
- [36] M. Jiang *et al.* (Super-Kamiokande), *PTEP* **2019**, 053F01 (2019), arXiv:1901.03230 [hep-ex].
- [37] V. Sitzmann, J. Martel, A. Bergman, D. Lindell, and G. Wetzstein, *Advances in neural information processing systems* **33**, 7462 (2020).
- [38] J. H. Hannay and J. F. Nye, *Journal of Physics A: Mathematical and General* **37**, 11591 (2004).
- [39] D. P. Kingma and M. Welling, “Auto-encoding variational bayes,” (2022), arXiv:1312.6114 [stat.ML].
- [40] Y. Bengio, N. Léonard, and A. Courville, “Estimating or propagating gradients through stochastic neurons for conditional computation,” (2013), arXiv:1308.3432 [cs.LG].
- [41] Y. Okajima *et al.*, *PoS PhotoDet2015*, 015 (2016).
- [42] K. Abe *et al.*, *Nucl. Instrum. Meth. A* **737**, 253 (2014), arXiv:1307.0162 [physics.ins-det].
- [43] D. P. Kingma and J. Ba (2014) arXiv:1412.6980 [cs.LG].
- [44] M. Jiang, *Study of the neutrino mass hierarchy with the atmospheric neutrino data collected in Super-Kamiokande IV*, *Ph.D. thesis*, Kyoto U. (2019).
- [45] B. Mildenhall, P. P. Srinivasan, M. Tancik, J. T. Barron, R. Ramamoorthi, and R. Ng, in *The European Conference on Computer Vision (ECCV)* (2020).
- [46] G. Papamakarios, E. Nalisnick, D. J. Rezende, S. Mohamed, and B. Lakshminarayanan, *J. Mach. Learn. Res.* **22** (2021).

Appendix A: SIREN Training Details

The surrogate model $f_{\gamma}^{\text{Cherenkov}}(E, s, \theta)$ is implemented as a Sinusoidal Representation Network (SIREN) [37], chosen for its ability to represent high-frequency features smoothly and differentially.

We generate the training data using PHOTONSIM, a GEANT4-based tool that simulates photon emission for monoenergetic charged particles in water. For each particle type, photon distributions are computed for $E \in [100, 2000]$ MeV in 10 MeV steps. Each energy point includes 10^4 simulated events, from which we extract two-dimensional histograms in $(s, \cos\theta)$. The resulting 3D lookup table $(E, s, \cos\theta)$ is normalized and log-transformed to enhance sensitivity to low-intensity regions.

The SIREN architecture consists of three input features (E, s, θ) , three hidden layers of 256 neurons each with sinusoidal activations, and a single linear output neuron. The output is squared to ensure non-negative photon intensities. We apply min-max normalization to the targets in the $[-1, 1]$ range and include a small fraction (0.2%) of zero-intensity samples to improve coverage.

Training is performed in JAX using the Adam optimizer with an initial learning rate of 10^{-4} and patience-based scheduling. The batch size is 65,536 elements, and training is conducted for 50k steps, sufficient for the mean squared error (MSE) loss to reach a stable plateau. We use a 90/10 train-validation split and store the model parameters at the minimum validation loss.

Appendix B: A surrogate for particle light emission in scintillator media

Extending the present work to include the modeling of scintillation light is a natural next step. Here we outline how such an extension could be implemented, to emphasize that there are no limitations preventing the application of the proposed method to any type of optical detector.

Modeling scintillation light emission requires parameterizing the deposited energy as a function of the distance along the particle track and the initial particle energy, $E_{\text{dep}}(s; E_{\text{track}})$. This system is conceptually simpler than the Cherenkov case because it involves one fewer dimension, as the photon emission angle does not need to be modeled. With this parameterization in place, the ray intensity could be computed as

$$I^{\text{scint}}(s, t_0) = f_{\gamma}^{t_0}(E_{\text{track}}, s) \times Y(E_{\text{dep}}), \quad (\text{B1})$$

where $Y(E_{\text{dep}})$ corresponds to Birks’ law:

$$Y(E_{\text{dep}}) = A \frac{dE_{\text{dep}}/ds}{1 + k_B (dE_{\text{dep}}/ds)}, \quad (\text{B2})$$

with A a normalization constant representing the light yield in the linear regime, and k_B the Birks constant. The

function f_γ^{to} would need to be parameterized to match the typical de-excitation time of the scintillator medium, τ_S .

Through this formulation, the expected distributions depend explicitly on A , k_B , and τ_S , allowing these parameters to be tuned using gradient-based optimization.

PHOTONSIM already includes utilities to generate the necessary inputs for $E_{\text{dep}}(s; E_{\text{track}})$, and the authors of this work welcome new contributions to extend LUCiD in this direction.

Appendix C: Adaptive Binning for Ray Generation

The Cherenkov emission profile $f_\gamma^{\text{Cherenkov}}(E, s, \theta)$ is concentrated in a relatively narrow region of the (s, θ) parameter space, while most of the domain yields negligible emission. Uniform random sampling over the full parameter range would therefore waste computational resources by generating sampling rays with negligibly small weights. To address this, we employ an adaptive binning strategy.

The method proceeds in two stages. First, we discretize the emission parameter space into a uniform $n \times n$ grid spanning the valid ranges of $s \in [0, s_{\text{max}}]$ and $\theta \in [0, \theta_{\text{max}}]$, where $n = 250$ by default. For a given particle energy E , the SIREN network is evaluated at all n^2 grid points to obtain the photon density $w_{ij} = f_\gamma^{\text{Cherenkov}}(E, s_i, \theta_j)$ at each bin center. An energy-dependent number of candidate bins is then selected according to

$$N_{\text{seeds}}(E) = \lfloor a E^b + c \rfloor, \quad (\text{C1})$$

where a , b , and c are empirically determined coefficients and E is in MeV. For each of the N_{rays} rays to be generated, a bin is drawn uniformly at random from the N_{seeds} highest-weighted bins.

The coefficients (a, b, c) are calculated parametrising the number of grid bins exceeding an intensity cutoff threshold w_{cut} as a function of energy. This threshold is chosen to exclude bins where the SIREN predicts negligible photon emission while retaining all physically significant contributions. By fitting a power law to the number of valid bins versus energy, we obtain parameters that ensure $N_{\text{seeds}}(E)$ tracks the true extent of the emission region across the full energy range. For muons in water, using $w_{\text{cut}} = 2$, the fit yields $a = 7.08$, $b = 0.87$, and $c = -334$ with $R^2 = 0.9997$.

In the second stage, stratified jittering is applied within each selected bin to ensure uniform coverage and reduce sampling variance. The bin interior along each dimension is partitioned into N_{rays} strata, which are randomly permuted and assigned to individual rays. Each ray receives a random offset within its stratum:

$$\delta_s = \left(\frac{\pi_s(i) + \epsilon_s}{N_{\text{rays}}} - \frac{1}{2} \right) \Delta_s, \quad \delta_\theta = \left(\frac{\pi_\theta(i) + \epsilon_\theta}{N_{\text{rays}}} - \frac{1}{2} \right) \Delta_\theta, \quad (\text{C2})$$

where π_s and π_θ are random permutations of $\{0, \dots, N_{\text{rays}} - 1\}$, $\epsilon_s, \epsilon_\theta \sim \mathcal{U}[0, 1]$ provide within-stratum jitter, and Δ_s, Δ_θ are the bin widths. The SIREN network is then re-evaluated at the refined positions $(s_i + \delta_s, \theta_i + \delta_\theta)$ to obtain the final per-ray weights.

Appendix D: Propagation

1. Reparameterized Functions

Here we detail the differentiable mappings $f(\epsilon; \theta)$ used to transform uniform noise $\epsilon \sim \mathcal{U}[0, 1]$ into physical quantities, as implemented in our JAX-based simulation.

a. Volumetric Scattering Distance

To sample a scattering distance d_s strictly within the detector volume bounded by d_{surf} , we employ a truncated exponential distribution. The normalized CDF is inverted to yield the differentiable mapping:

$$d_s(\epsilon, \lambda_s) = -\lambda_s \ln \left(1 - \epsilon \left(1 - e^{-d_{\text{surf}}/\lambda_s} \right) \right). \quad (\text{D1})$$

This formulation ensures $0 \leq d_s \leq d_{\text{surf}}$ while preserving gradient flow from the interaction point back to the scattering length λ_s .

b. Rayleigh Scattering Angle

For Rayleigh scattering, the cumulative distribution function for the cosine of the scattering angle $\mu = \cos \theta$ leads to the cubic equation:

$$\mu^3 + 3\mu + 4(1 - 2\epsilon) = 0. \quad (\text{D2})$$

Standard rejection sampling is non-differentiable. Instead, we obtain μ by solving this cubic equation analytically using Cardano's formula. This provides a closed-form, differentiable expression for the scattering angle as a function of the uniform noise ϵ .

c. Lambertian Reflection

We simulate diffuse reflection by mapping two noise samples ϵ_1, ϵ_2 to a cosine-weighted hemisphere. The local vector is constructed as:

$$\mathbf{u}_{\text{local}} = \left[\sqrt{\epsilon_1} \cos(2\pi\epsilon_2), \sqrt{\epsilon_1} \sin(2\pi\epsilon_2), \sqrt{1 - \epsilon_1} \right]^T. \quad (\text{D3})$$

This vector is then rotated into the global frame using a basis derived from the surface normal \mathbf{n} , allowing gradients to propagate through the surface orientation.

Algorithm 1. Differentiable Ray Propagation

Input: Ray states $\Psi = \{(\mathbf{x}_i, \mathbf{u}_i, t_i, I_i)\}_{i=1}^N$, Parameters θ
Output: Deposition List \mathcal{D}

- 1: Initialize $\mathcal{D} \leftarrow \emptyset$, Survival factors $\alpha \leftarrow \mathbf{1}$
- 2: **for** $k \leftarrow 1$ **to** K **do**
- 3: **1. Intersection & Probabilities**
- 4: $c_{\text{grid}} \leftarrow \text{MapToGrid}(\mathbf{x}_i, \mathbf{u}_i)$
- 5: $S_{\text{candidates}} \leftarrow \text{GridLookup}(c_{\text{grid}})$
- 6: $d_{\text{surf}}, \mathbf{n}, \text{type} \leftarrow \text{AnalyticIntersect}(\Psi)$
- 7: $P_{\text{reach}} \leftarrow \exp(-d_{\text{surf}}/\lambda_s)$
- 8: $P_{\text{scat}} \leftarrow 1 - P_{\text{reach}}$
- 9: $R \leftarrow (\text{type} == \text{Sensor})?R_s : R_w$
- 10: $P_{\text{det}} \leftarrow P_{\text{reach}}(1 - R), \quad P_{\text{ref}} \leftarrow P_{\text{reach}}R$
- 11: **2. Deposition (Implicit Capture)**
- 12: **Parallel for** each candidate sensor $j \in S_{\text{candidates}}$:
 - 13: $b \leftarrow \text{DistClosestApproach}(\mathbf{x}_i, \mathbf{u}_i, \text{Sensor}_j)$
 - 14: $w_{\text{geo}} \leftarrow \text{OverlapIntegral}(b, \sigma)$ ▷ See Sec. IID3
 - 15: $n_{\text{dep}} \leftarrow I_i \cdot \alpha_i \cdot P_{\text{det}} \cdot e^{-d_{\text{surf}}/\lambda_a} \cdot w_{\text{geo}}$
 - 16: $t_{\text{hit}} \leftarrow t_i + d_{\text{surf}}/v_{\text{group}}$
 - 17: $\mathcal{D}.\text{append}(\{\text{sensor} : j, \text{step} : k, \text{photons} : n_{\text{dep}}, \text{time} : t_{\text{hit}}\})$
- 18: **3. Propagation (Differentiable Branching)**
- 19: *Path A: Volumetric Scattering*
 - 20: $\epsilon_d, \epsilon_\theta \sim \mathcal{U}[0, 1]$ ▷ Sample fixed noise
 - 21: $d_s \leftarrow -\lambda_s \ln(1 - \epsilon_d(1 - e^{-d_{\text{surf}}/\lambda_s}))$ ▷ Truncated Exp (App. D1)
 - 22: $\mathbf{x}_s \leftarrow \mathbf{x}_i + d_s \hat{\mathbf{u}}_i$
 - 23: $\mu_s \leftarrow \text{RayleighInverseCDF}(\epsilon_\theta)$ ▷ Cubic solver (App. D1)
 - 24: $\mathbf{u}_s \leftarrow \text{Rotate}(\mathbf{u}_i, \mu_s)$
- 25: *Path B: Surface Reflection*
 - 26: $\mathbf{x}_r \leftarrow \mathbf{x}_i + d_{\text{surf}} \hat{\mathbf{u}}_i + \delta \hat{\mathbf{n}}$ ▷ $\delta \ll 1$: nudge off surface
 - 27: $\mathbf{u}_{\text{spec}} \leftarrow \text{ReflectSpecular}(\mathbf{u}_i, \mathbf{n})$
 - 28: $\epsilon_{1,2} \sim \mathcal{U}[0, 1]$
 - 29: $\mathbf{u}_{\text{diff}} \leftarrow \text{SampleLambertian}(\mathbf{n}, \epsilon_{1,2})$ ▷ Cosine-weighted (App. D1)
 - 30: $\mathbf{u}_r \leftarrow (\text{type} == \text{Sensor})?\mathbf{u}_{\text{spec}} : \mathbf{u}_{\text{diff}}$
- 31: *Path Selection (Straight-Through Estimator)*
 - 32: $\mathbf{P} \leftarrow [P_{\text{scat}}, P_{\text{ref}}]/(P_{\text{scat}} + P_{\text{ref}})$
 - 33: $\mathbf{h} \sim \text{Categorical}(\mathbf{P})$ ▷ One-hot sample
 - 34: $\mathbf{w} \leftarrow \mathbf{h} - \text{sg}(\mathbf{P}) + \mathbf{P}$ ▷ Stop-gradient trick
 - 35: $d_{\text{step}} \leftarrow w_0 d_s + w_1 d_{\text{surf}}$
 - 36: $\mathbf{x}_{\text{new}} \leftarrow w_0 \mathbf{x}_s + w_1 \mathbf{x}_r$
 - 37: $\mathbf{u}_{\text{new}} \leftarrow w_0 \mathbf{u}_s + w_1 \mathbf{u}_r$
- 38: **4. Update State**
- 39: $\mathbf{x}_i \leftarrow \mathbf{x}_{\text{new}}, \quad \mathbf{u}_i \leftarrow \mathbf{u}_{\text{new}}$
- 40: $t_i \leftarrow t_i + d_{\text{step}}/v_{\text{group}}$
- 41: $\alpha_i \leftarrow \alpha_i \cdot \exp(-d_{\text{step}}/\lambda_a)$ ▷ Continuous absorption weight
- 42: **end for**
- 43: **return** \mathcal{D}

2. Spatial Overlap Integral

The photon relaxation weight w_{geo} represents the probability of a Gaussian photon packet striking a circular sensor of radius r . We define the integral in polar coordinates (ρ, ϕ) centered on the sensor, where the photon is incident at a distance b from the center:

$$\mathcal{I}(b) = \int_0^r \int_0^{2\pi} \frac{\rho}{2\pi\sigma^2} \exp\left(-\frac{\rho^2 + b^2 - 2\rho b \cos \phi}{2\sigma^2}\right) d\phi d\rho. \quad (\text{D4})$$

Evaluating this double integral during propagation is computationally expensive. Instead, we precompute the

function $\mathcal{I}(b)$ and store it as a 1D lookup table. To maintain high precision while minimizing memory usage, we do not use a uniform grid. The function $\mathcal{I}(b)$ changes most rapidly near the sensor edge ($b \approx r$), where it transitions from ≈ 1 to ≈ 0 . We therefore construct a non-uniform grid for b with three distinct regions:

1. Inner Sparse Region ($0 \leq b < r - 3\sigma$): The overlap is near-unity and flat; we use sparse sampling here.
2. Transition Region ($|b - r| \leq 3\sigma$): The overlap drops sharply; we use a denser grid to capture the gradient accurately.
3. Outer Sparse Region ($b > r + 3\sigma$): The overlap tails

Algorithm 2. Monte Carlo Ray Propagation (Sampling Mode)

Input: Ray states $\Psi = \{(\mathbf{x}_i, \mathbf{u}_i, t_i)\}_{i=1}^N$, Parameters θ
Output: Hit List \mathcal{H}

- 1: Initialize $\mathcal{H} \leftarrow \emptyset$
- 2: **for** $k \leftarrow 1$ **to** K **do**
- 3: **1. Intersection & Probabilities**
- 4: $d_{\text{surf}}, \mathbf{n}, \text{type} \leftarrow \text{AnalyticIntersect}(\mathbf{x}_i, \mathbf{u}_i)$
- 5: $P_{\text{reach}} \leftarrow \exp(-d_{\text{surf}}/\lambda_s)$
- 6: $R \leftarrow (\text{type} == \text{Sensor}) ? R_s : R_w$
- 7: **2. Outcome Sampling & Propagation**
- 8: *Sample interaction type:*
- 9: $\epsilon_1 \sim \mathcal{U}[0, 1]; \text{reaches_surface} \leftarrow (\epsilon_1 < P_{\text{reach}})$
- 10: $\epsilon_2 \sim \mathcal{U}[0, 1]$
- 11: $\text{detect} \leftarrow \text{reaches_surface and } \epsilon_2 \geq R$
- 12: $\text{reflect} \leftarrow \text{reaches_surface and } \epsilon_2 < R$
- 13: $\text{scatter} \leftarrow \text{not reaches_surface}$
- 14: *Scatter path:*
- 15: $\epsilon_d \sim \mathcal{U}[0, 1]$
- 16: $d_s \leftarrow -\lambda_s \ln(1 - \epsilon_d(1 - e^{-d_{\text{surf}}/\lambda_s}))$
- 17: $\epsilon_\theta, \epsilon_\phi \sim \mathcal{U}[0, 1]$
- 18: $\mu_s \leftarrow \text{RayleighInverseCDF}(\epsilon_\theta); \mathbf{u}_s \leftarrow \text{Rotate}(\mathbf{u}_i, \mu_s, 2\pi\epsilon_\phi)$
- 19: *Reflection path:*
- 20: $\mathbf{u}_r \leftarrow \text{ReflectSpecular}(\mathbf{u}_i, \mathbf{n})$
- 21: *Hard selection:*
- 22: **if** scatter **then**
- 23: $\mathbf{x}_{\text{new}} \leftarrow \mathbf{x}_i + d_s \hat{\mathbf{u}}_i$
- 24: $\mathbf{u}_{\text{new}} \leftarrow \mathbf{u}_s$
- 25: $d_{\text{step}} \leftarrow d_s$
- 26: **else**
- 27: $\mathbf{x}_{\text{new}} \leftarrow \mathbf{x}_i + d_{\text{surf}} \hat{\mathbf{u}}_i + \delta \hat{\mathbf{n}}$ $\triangleright \delta \ll 1: \text{ nudge off surface}$
- 28: $\mathbf{u}_{\text{new}} \leftarrow \mathbf{u}_r$
- 29: $d_{\text{step}} \leftarrow d_{\text{surf}}$
- 30: *Absorption survival:*
- 31: $\epsilon_3 \sim \mathcal{U}[0, 1]; \text{survives} \leftarrow (\epsilon_3 < \exp(-d_{\text{step}}/\lambda_a))$
- 32: **3. Record & Update**
- 33: $\mathbf{x}_i \leftarrow \mathbf{x}_{\text{new}}, \mathbf{u}_i \leftarrow \mathbf{u}_{\text{new}}$
- 34: $t_i \leftarrow t_i + d_{\text{step}}/v_{\text{group}}$
- 35: **if** detect **and** survives **then**
- 36: $\mathcal{H}.\text{append}(\{\text{sensor} : \text{id}(\mathbf{n}), \text{time} : t_i\})$
- 37: **if** detect **or** not survives **then**
- 38: $\text{weight} \leftarrow 0$
- 39: **end for**
- 40: **return** \mathcal{H}

off to zero; we use sparse sampling up to a cutoff distance (e.g., $10r$).

We typically use 150 points for the transition region and 50 points for the inner and outer sparse regions accordingly. During simulation, the value of w_{geo} is retrieved via linear interpolation of this lookup table. This operation is fully differentiable, allowing gradients to propagate through the lookup values with respect to the impact parameter b .

3. Convergence of Propagation Depth

The computational cost of the simulation scales linearly with the maximum number of propagation itera-

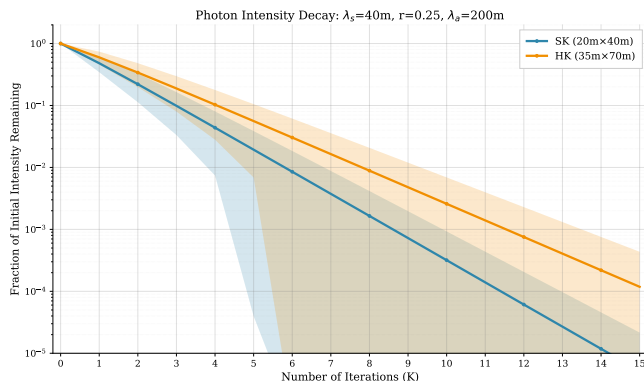
tions, K . It is therefore crucial to select a value of K that minimizes computational overhead while ensuring that the total neglected photon intensity remains negligible.

To determine the optimal cutoff, we simulated the propagation of light from an isotropic point source placed at the center of two detector geometries: an SK-like variant geometry ($20 \text{ m} \times 40 \text{ m}$) and an HK-like variant geometry ($35 \text{ m} \times 70 \text{ m}$). We utilized a representative set of optical parameters: a scattering length $\lambda_s = 40 \text{ m}$, an absorption length $\lambda_a = 200 \text{ m}$, and a surface reflection rate $R = 0.25$.

Figure 17 shows the fraction of the initial photon intensity remaining in the simulation queue as a function of the iteration index k . The intensity decays exponentially as photons are absorbed by the medium or detected by the

photosensors. For the SK-like geometry, we observe that at $K = 8$, the average remaining intensity drops below 0.2% (10^{-3}). This threshold serves as our convergence criterion. Larger detector volumes, such as the HK-like geometry, exhibit a slightly slower decay rate due to the longer average path lengths between surface interactions, yet they follow a similar convergence profile.

FIG. 17. The fraction of initial photon intensity remaining active in the simulation as a function of the number of propagation iterations (K).



Appendix E: Track Initial Guesses

Stage 0: Initial Energy Estimation. An initial estimate of the particle energy is obtained by minimizing the difference between the observed and predicted total photoelectron counts. The energy scan evaluates 10 trial values in the range $[E_0 - 700, E_0 + 700]$ MeV, where E_0 is chosen randomly from a uniform distribution in the interval $[E_0 - 50, E_0 + 50]$ MeV. This randomization prevents fine-tuning of the reported performance when analyzing monochromatic samples. During this stage, the track origin is fixed at the detector center, and the track direction is set to the arbitrary unit vector $\mathbf{d} = (1/\sqrt{3}, 1/\sqrt{3}, 1/\sqrt{3})$. Since the evaluation metric depends only on the total signal normalization and not on the detailed charge pattern, the specific choice of position and direction is not critical. The chosen configuration, however, ensures that counts are distributed across multiple detector surfaces for most geometries.

Stage 1: Position and Time Offset Search. A hierarchical grid search determines the vertex position and time offset t_0 simultaneously. The algorithm evaluates 30 uniformly spaced t_0 values in the range $[-15, 15]$ ns. For each t_0 , a complete three-dimensional hierarchical position search is performed as follows:

- The search begins at the detector center with a cubic grid spanning the detector volume.
- Each spatial dimension is divided into $n_{\text{div}} = 5$ intervals with an initial grid spacing L .
- The time loss is evaluated at every grid point.
- The search is refined hierarchically over 6 levels.
- At each level, the grid is re-centered on the best position from the previous iteration, with the search region half-size set to $L/2$, and a new spacing defined as $L_{\text{new}} = L/n_{\text{div}}$.

The position and t_0 combination yielding the minimum loss over all tested t_0 values is selected as the best estimate.

Stage 2: Direction Search. A hierarchical cone-based search determines the particle direction through the following steps:

- Global sampling is performed with 5 divisions in polar angle $\theta \in [0, \pi]$ and 10 divisions in azimuthal angle $\phi \in [0, 2\pi)$, forming a uniform angular grid.
- For each sampled direction, the loss $\mathcal{L}_{\text{counts}}$ between observed and simulated photon counts is evaluated.
- Around the best-performing direction from the global scan, a cone with opening angle $\alpha_{\text{max}} = 30^\circ$ is generated. It is populated by four concentric rings of points, with the number of points per ring increasing with radius to maintain uniform angular spacing.

The direction minimizing $\mathcal{L}_{\text{counts}}$ across all tested directions is selected as the best estimate.

Stage 3: Final Energy Estimation. Finally, a linear scan over 25 energy values in the range $[E_{\text{guess}} - 400, E_{\text{guess}} + 400]$ MeV is performed, using the position and direction estimates obtained from Stages 1 and 2. The energy value that minimizes the loss is selected as the final energy estimate.